https://doi.org/10.5194/egusphere-2026-1065
Preprint. Discussion started: 7 April 2026

Evolution of L-band SAR Response for Soil Freeze/Thaw Monitoring: A Case Study Over Snow-Covered Canadian Mid-latitude Agricultural Region

Zeinab Akhavan[1], Richard Kelly[1], Peter Toose[2], Aaron Thompson[3], Wei Wang[1], Benoit Montpetit[2], Alex Gélinas[4], and Alexandre Roy[4]

[1]Department of Geography and Environmental Management, University of Waterloo, Waterloo, Ontario, Canada
[2]Climate Research Division, Environment and Climate Change Canada, Ontario, Canada
[3]Geological Survey of Canada, Natural Resources Canada, Ontario, Canada
[4]Department of Environmental Sciences, University of Quebec in Trois-Rivières, Quebec, Canada

Correspondence: Zeinab Akhavan (z2akhava@uwaterloo.ca)

Abstract. Soil freeze/thaw (F/T) cycles are critical regulators of global hydrological and biogeochemical processes, yet monitoring these subsurface dynamics beneath snow cover remains a significant observational challenge. There is a corresponding need for physically-based retrieval frameworks to support upcoming spaceborne Earth observation missions, such as the NASA-ISRO Synthetic Aperture Radar (NISAR) mission. Despite the importance of these cycles, there remains a critical lack of understanding regarding L-band Synthetic Aperture Radar (SAR) response beneath snow cover, primarily resulting from a reliance on coarse-resolution data and a lack of coincident, season-long ground validation. To address this, we introduce an integrated physical framework that couples high-resolution (1 m) airborne L-band (1.3 GHz) observations with coincident in situ measurements of soil temperature and permittivity. This approach utilizes analysis of backscatter responses, Freeman-Durden polarimetric decomposition, and the Improved Integral Equation Model (I^2EM) to physically interpret microwave scattering and characterize subnivean F/T transitions under frozen and thawed conditions. VV-polarized backscatter exhibited the strongest sensitivity to F/T transitions, increasing during thaw and decreasing under frozen soil. Decomposition analysis revealed dominant surface scattering under frozen conditions, increased surface scattering during thaw, and enhanced volume scattering associated with melt–refreeze cycles. The I^2EM simulations captured the VV and HV backscatter trends within an acceptable range across most soil stations, while significantly underestimating the HH backscatter. Overall, these results advance process-level understanding of the L-band SAR response to subnivean soil F/T transitions and demonstrate the potential of high-resolution observations for improving retrieval algorithms and calibrating forthcoming global L-band satellite missions.

1 Introduction

Soil freeze/thaw (F/T) cycles are prevalent across much of the northern hemisphere above 45°N, occurring as either brief diurnal shifts or prolonged seasonal transitions (Rowlandson et al., 2018). The timing and spatial distribution of these transitions influence key hydrological processes, as well as terrestrial carbon, water, and energy balances. The F/T status of soil also affects

https://doi.org/10.5194/egusphere-2026-1065
Preprint. Discussion started: 7 April 2026

vegetation productivity, particularly in boreal and subarctic ecosystems (Kim et al., 2017; Mavrovic et al., 2023; Rowlandson et al., 2018; Mavrovic et al., 2024). Understanding seasonal and interannual variability in soil F/T dynamics is, therefore, critical for evaluating their broader climate impacts and for assessing carbon cycle feedbacks in northern regions (Prince et al., 2019; Zhou et al., 2021). Beneath the snow layer, the soil's F/T condition determines whether meltwater or rainwater infiltrates the ground or contributes to surface runoff. Accurate characterization of subnivean soil F/T state is essential for improving flood forecasting during seasonal snowmelt and for mitigating associated hydrological hazards (Bateni et al., 2015). Moreover, several snowpack properties, including density, depth, and microstructure, influence the transmission of thermal energy through the snow and subsequently affect the F/T transitions of the underlying soil layer (Prince et al., 2019; Crevier et al., 2025).

Due to the limited spatial and temporal coverage of in situ soil monitoring networks, recent efforts have increasingly leveraged remote sensing techniques to investigate the F/T state of soil beneath snow cover. Microwave remote sensing, both passive and active, has been applied for this purpose (Bateni et al., 2015; Prince et al., 2019; Rowlandson et al., 2018; Cohen et al., 2021). The active microwave backscatter from snow-covered surfaces is inherently complex and frequency dependent. At higher frequencies such as Ku- or Ka-band, the radar response is dominated by scattering from the air–snow interface and the snow volume, with additional contributions from snow–ground interactions depending on snow depth and physical properties. As a result, these higher frequencies may exhibit limitations in sensitivity to subnivean soil scattering due to attenuation and multiple scattering within the snowpack, although soil contributions may still be detectable under shallow snow conditions (Dagurov et al., 2020; Thompson and Kelly, 2021). In contrast, at lower frequencies such as L-band, snow generally has a low impact on radar backscatter due to its relatively long wavelength.

Selecting an appropriate SAR configuration for soil F/T monitoring thus requires careful consideration of both frequency and polarization (Cohen et al., 2021). High-frequency bands such as Ku-band (17.2 GHz) and, to a lesser extent, X-band (9.6 GHz), are particularly sensitive to snow characteristics like grain size and microstructure, making them less useful for soil F/T monitoring even in shallow snow conditions (Du et al., 2010; Lievens et al., 2022; Tsang et al., 2021). On the other hand, lower-frequency signals such as L-band experience minimal scattering from dry snow, as the snow grain size is much smaller than the L-band wavelength (Deeb et al., 2011; Marshall et al., 2021; Palomaki and Sproles, 2023; Shi et al., 2016). Moreover, L-band SAR can penetrate vegetation canopies and is less affected by surface vegetation, enabling deeper interaction with the underlying soil (Bahrami et al., 2022; Akhavan et al., 2021). These characteristics make L-band particularly well-suited for observing soil F/T transitions beneath snow cover (Cohen et al., 2021). The simplified schematic representation of the interaction between L-, X-, and Ku-band SAR signals and snow-covered soil is shown in Fig. 1. The actual SAR interactions, however, are more complex than this simplified respresentation. For instance, SAR signals can penetrate the soil when it is frozen or when thawed soil has low moisture content. While X-band signals are capable of penetrating frozen bare soil, they do not effectively penetrate vegetated surfaces, where the dominant backscatter response typically originates from the vegetation layer or the soil surface (Karam et al., 1992).

https://doi.org/10.5194/egusphere-2026-1065
Preprint. Discussion started: 7 April 2026

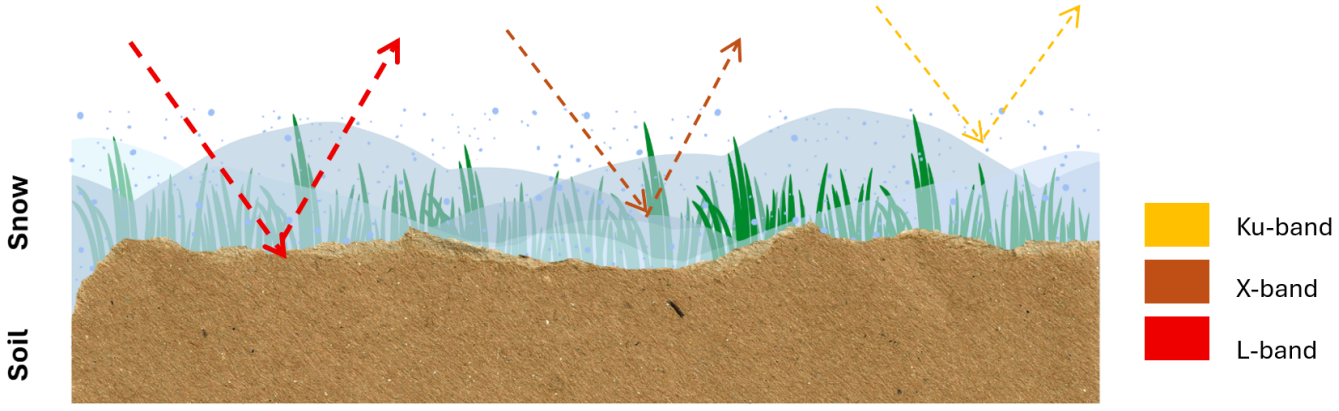

Figure 1. Schematic representation of L-, X-, and Ku-band radar signals penetrating a snow-covered soil surface, highlighting differences in interaction with the snow and underlying soil.

The relative permittivity ($\epsilon = \epsilon' - i\,\epsilon''$) of soil reflects the material's physical properties and its ability to absorb or scatter electromagnetic signals (Tsang et al., 2021). For L-band SAR, the imaginary component is negligible under dry snow conditions and can be omitted. The relative permittivity undergoes substantial changes when soil transitions between frozen and thawed states. As demonstrated in previous studies (Mavrovic et al., 2018; Mätzler, 1987), at L-band, freezing of water produces a strong contrast between the dielectric properties of water and ice. The relative permittivity is strongly dependent on, and increases with, volumetric moisture content (Long and Ulaby, 2015).

Polarimetric SAR decomposition techniques have been used to investigate the F/T state of soils, demonstrating that variations in the relative permittivity of a soil can be effectively monitored (Jagdhuber et al., 2014). These methods, grounded in physical scattering models, not only enable the detection of F/T transitions but also provide insight into the underlying scattering mechanisms (Jagdhuber et al., 2014; Park, 2015). Pioneering work by (Jagdhuber et al., 2014) utilized the H/A/α decomposition framework to capture changes in scattering behavior associated with soil phase transitions. Similarly, (Zhou et al., 2021) applied the dual-polarimetric H/α approach across summer and winter seasons, highlighting how seasonal variations correspond to shifts in scattering mechanisms.

Scattering models have also been used to analyze the contribution of the soil layer to SAR backscatter. These models are primarily categorized into theoretical, semi-empirical, and empirical approaches. Models such as the Integral Equation Model (IEM) (Fung et al., 1992), Oh model (Oh et al., 2002), and Dubois model (Dubois et al., 1995) have been extensively used to retrieve soil moisture over bare surfaces or areas with low vegetation cover. Previous studies highlight the need for accurate parameterization and reveal the computational complexity associated with theoretical models, while also noting that semi-empirical and empirical approaches often yield site-dependent results (Panciera et al., 2013). The Improved Integral Equation Model (I^2EM) model improves on the original IEM by refining surface scattering calculations, providing more accurate predictions for varying angles and small surface roughness while retaining an algebraic form, making it well suited for diverse soil conditions (Fung et al., 2002).

https://doi.org/10.5194/egusphere-2026-1065
Preprint. Discussion started: 7 April 2026

This study investigates seasonal soil F/T state transitions over an agricultural field in a mid-latitude Canadian environment using a dense time series of L-band airborne polarimetric SAR images, with an emphasis on the continuous seasonal evolution and variability of SAR responses throughout the winter period. This study was designed to address three objectives: (1) characterize the temporal patterns of high and low VV co-polarized backscatter and their variability; (2) assess temporal changes in L-band polarimetric parameters, focusing on high and low response levels and variability of surface and volume scattering components derived from Freeman–Durden decomposition analysis throughout the winter season; and (3) compare I^2EM forward estimates with L-band observations of the field site under frozen and thawed conditions throughout the winter season.

2 Material and Methods

2.1 Study Site

The field campaign was conducted between November 2022 and January 2024. The main goal of the campaign was to evaluate the potential of L-band fully polarimetric SAR observations to monitor the F/T state of soil beneath snow cover in an agricultural setting in Ontario, Canada (Kelly et al., 2024). To do so, the airborne Cryospheric SAR (CryoSAR) instrument (see Fig. 2) was used (Kelly et al., 2024). The study area (see Fig. 2), encompasses approximately 1500 m × 1000 m and is centered at 46.08°N, 79.34°W. The site includes a heterogeneous landscape consisting of open pasture fields in various stages of grazing, ploughed and planted cropland, as well as patches of mixed deciduous and coniferous forest. Soils across the study area consist of organic, clay, silt, and sand fractions, with silt being the dominant component. Six soil monitoring stations were deployed across the study area, and their locations are indicated in Fig. 2-b as Stations 1–6. The corresponding site names and geographic coordinates for these stations are listed in Table 1.

According to 1981–2010 climate normals from the nearest Environment and Climate Change Canada (ECCC) weather station located at 46.07°N, 79.15°W, daily temperatures in the region average a maximum of 24.9 in July and a minimum of -17.7 in January. Precipitation occurs predominantly as snow between October and May, with the highest monthly average snowfall reaching 48.3 cm in January (Environment and Climate Change Canada, 2024).

https://doi.org/10.5194/egusphere-2026-1065
Preprint. Discussion started: 7 April 2026

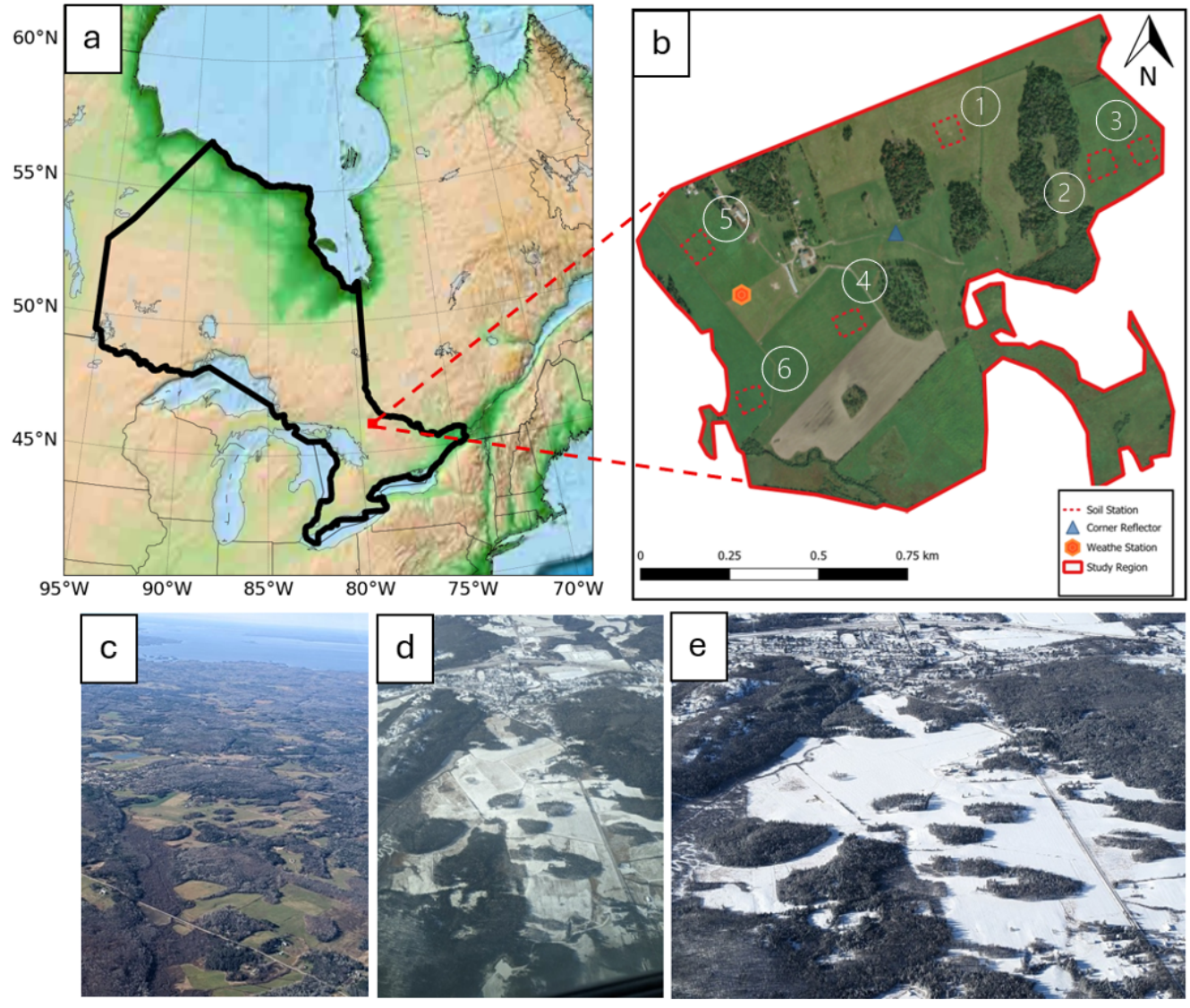

Figure 2. Overview of the study area. (a) Regional map showing the portion of Canada that includes the study site. (b) Detailed boundary of the CryoSAR field campaign area in Ontario. (c-e) Airborne views of the field site captured during the campaign in October 2022 (c), November 2022 (d), and January 2023 (e).

https://doi.org/10.5194/egusphere-2026-1065
Preprint. Discussion started: 7 April 2026

Table 1. List of the soil stations deployed across the study area, including their assigned station numbers, names, and geographic coordinates.

No.	Station	Latitude	Longitude
1	Central	46° 5’20.91"N	79°20’28.35"W
2	East Dry	46° 5’18.91"N	79°20’4.00"W
3	Eastern	46° 5’18.17"N	79°20’9.21"W
4	Lower	46° 5’3.92"N	79°20’40.81"W
5	Upper	46° 5’10.83"N	79°20’59.89"W
6	Winter Rye	46° 4’57.40"N	79°20’52.94"W

2.2 CryoSAR Polarimetric SAR Observations

L-band (1.3 GHz) fully polarimetric SAR data were acquired as part of the CryoSAR airborne campaign to investigate soil conditions beneath a snowpack at the field site. The CryoSAR instrument was mounted on the rear cargo doors which were installed on Cessna 208B Grand Caravan aircraft based out of the Muskoka airport (YQA) (Fig. 3-a and b). The airborne radar data were collected along predefined flight lines, with repeat passes conducted during the same flight and between flight campaigns over the same area to support reproducible temporal analysis. The CryoSAR system parameters are summarized in Table 2. An 80cm L-band square trihedral corner reflector was installed at the study site for radiometric and polarimetric calibration (Fig. 3-c).

https://doi.org/10.5194/egusphere-2026-1065
Preprint. Discussion started: 7 April 2026

Table 2. L-band CryoSAR system parameters.

Parameter	L-band (1.3 GHz)
Bandwidth (max)	200 MHz
Acquisition modes	Quad-pol
Azimuth resolution (max)	25 cm
Tx power (max)	10 W (40 dBm)
Cross-pol isolation | NESZ	< -28 dB | < -32 dB
Transmit stability	< 0.05 dB
Antenna gain	13 dB
Radiometric calibration accuracy	1 dB
HPBW (el $\times$ Az)	$40^\circ \times 40^\circ$
Transmit PRF (max)	20 kHz

A total of ten single-look complex (SLC) Level-1 images with full polarimetric channels (HH, HV, VH, VV) were collected over two winters, between November 2022 and January 2024, with the most frequent flights occurring between January and March 2023 (Table 3). Each image has a spatial resolution of 1 m × 1 m. The acquisition from 24 November 2023 was selected to represent snow-free conditions, under the assumption of comparable environmental settings across corresponding dates in consecutive years.

Table 3. L-band CryoSAR acquisition dates over two winters 2023-2024

Date	
2023/01/14	2023/01/31
2023/02/14	2023/02/24
2023/03/01	2023/03/03
2023/03/15	2023/03/30
2023/11/24	2024/01/12

The CryoSAR data was processed from raw measurements to Level-1 SLC products using MetaSARPro software (De Macedo et al., 2021). The raw dataset included the associated Global Navigation Satellite System (GNSS) navigation and configuration files recorded onboard the aircraft during flight, organized by frequency and polarization channel (e.g., HH, HV, VH, VV). Post-processing of the aircraft's position used the onboard GNSS antenna–generated files, which were corrected using a nearby network-accessible base station. The accuracy of the aircraft's trajectory was further improved by combining the on-

https://doi.org/10.5194/egusphere-2026-1065
Preprint. Discussion started: 7 April 2026

board GNSS data and the CryoSAR's integrated Inertial Measurement Unit (IMU). The refined navigation solution was used to geolocate the SAR imagery. Range compression was performed using a Fast Fourier Transform (FFT) to generate Range-Doppler maps. Motion compensation and range migration corrections were applied using a Ground Back-Projection algorithm, resulting in Level-1 georeferenced SLC imagery containing both amplitude (A) and phase (ϕ) information.

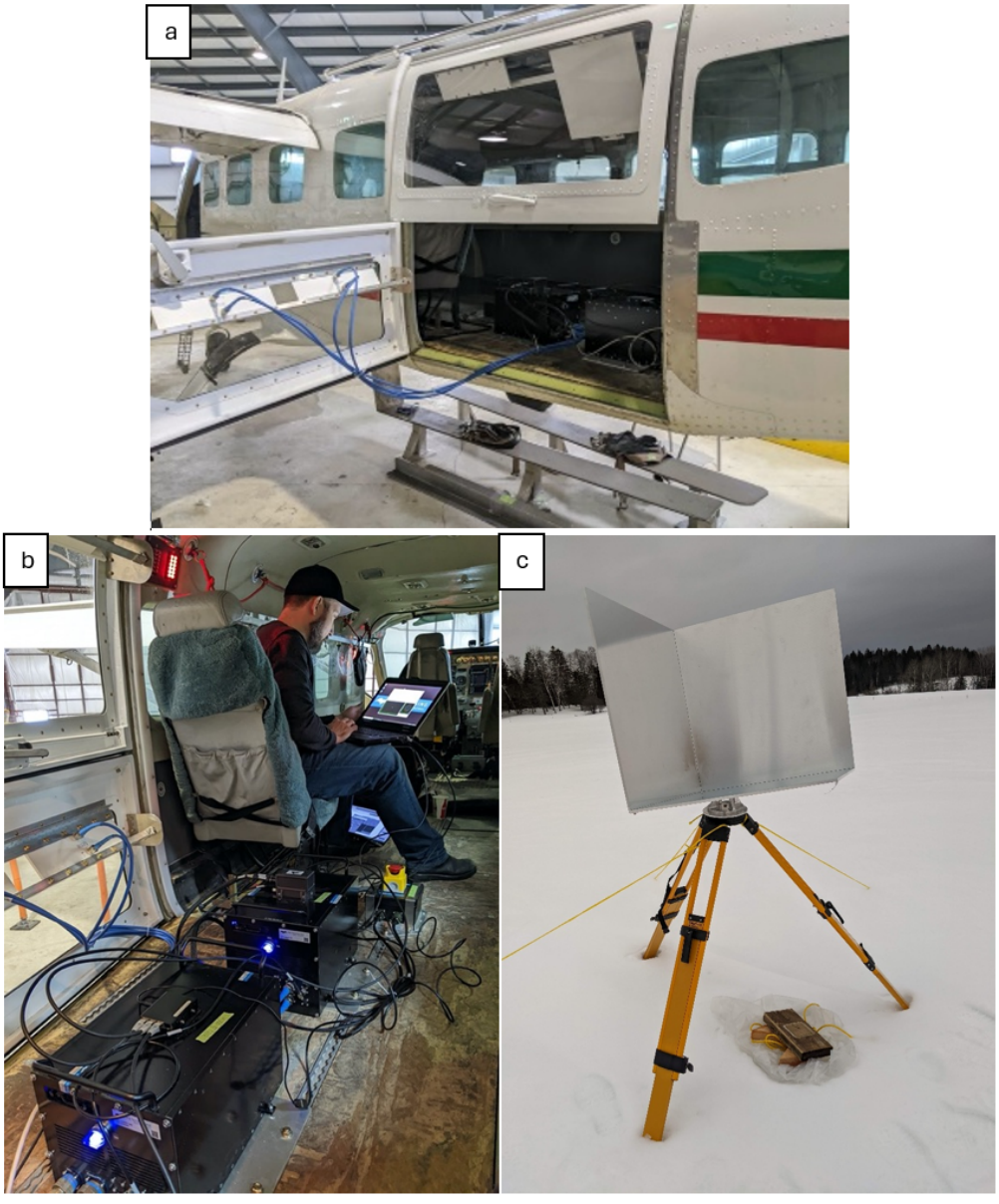

Figure 3. CryoSAR system and field calibration setup. (a, b) The CryoSAR instrument mounted on the Cessna 208B Grand Caravan aircraft. (c) An L-band corner reflector deployed at the field site for calibration purposes.

https://doi.org/10.5194/egusphere-2026-1065
Preprint. Discussion started: 7 April 2026

To normalize the received power and mitigate the effects of antenna radiation patterns due to changing in-flight instrument viewing geometry, geometric and radiometric calibrations were performed using an in-scene corner reflector. The calibration accuracy for the L-band data was found to be approximately 1.0 dB (see Table 2). The calibrated dataset was exported to a netCDF format for subsequent analysis. Further processing, including generation of the scattering matrix, covariance matrix, and additional CryoSAR data analyses, was conducted using MATLAB 2024b and the Python Programming Language.

2.3 In situ Data

A field experiment was conducted over two winters, between October 2022 and April 2023 and again from October 2023 to January 2024, at the study site, providing coincident in situ measurements of soil, snow, and meteorological conditions to support the analysis of L-band backscatter and its relation to snow cover and underlying soil properties. Measurements of the real permittivity parameters, which is directly related to soil moisture, and soil temperature were collected throughout the season (Fig. 4-a and b and Fig. 7) to characterize changes in surface and subsurface conditions. In addition, meteorological observations were obtained from an Onset U30 HOBO weather station (Fig. 4-a and Fig. 5) to complement the soil measurements. It should be noted that this meteorological station was non-operational between 21 December 2022 and 10 January 2023, although there were no SAR acquisitions during this period.

Six soil stations were installed at various locations across the study site (Fig. 4-b). At each station, two Stevens HydraProbes were vertically embedded in the soil to monitor real dielectric permittivity (70 MHz) and temperature at a depth of 0-5.7 cm (Fig. 4-c). A single Onset U30 HOBO weather station was installed to monitor air temperature and relative humidity, snow depth and temperature, and wind speed and direction. All soil and meteorological sensors were logged at 30-minute intervals, enabling the capture of rapid transitions between F/T states. The stations were spatially distributed to represent a range of field conditions, including pasture land with different grazing intensities, a recently ploughed field, and regions with varying moisture levels (wet and dry zones of the fields). To ensure consistency in measurements, each station was placed in a relatively homogeneous area, typically near the center of open fields and away from field edges, which are known to influence snow deposition patterns.

https://doi.org/10.5194/egusphere-2026-1065
Preprint. Discussion started: 7 April 2026

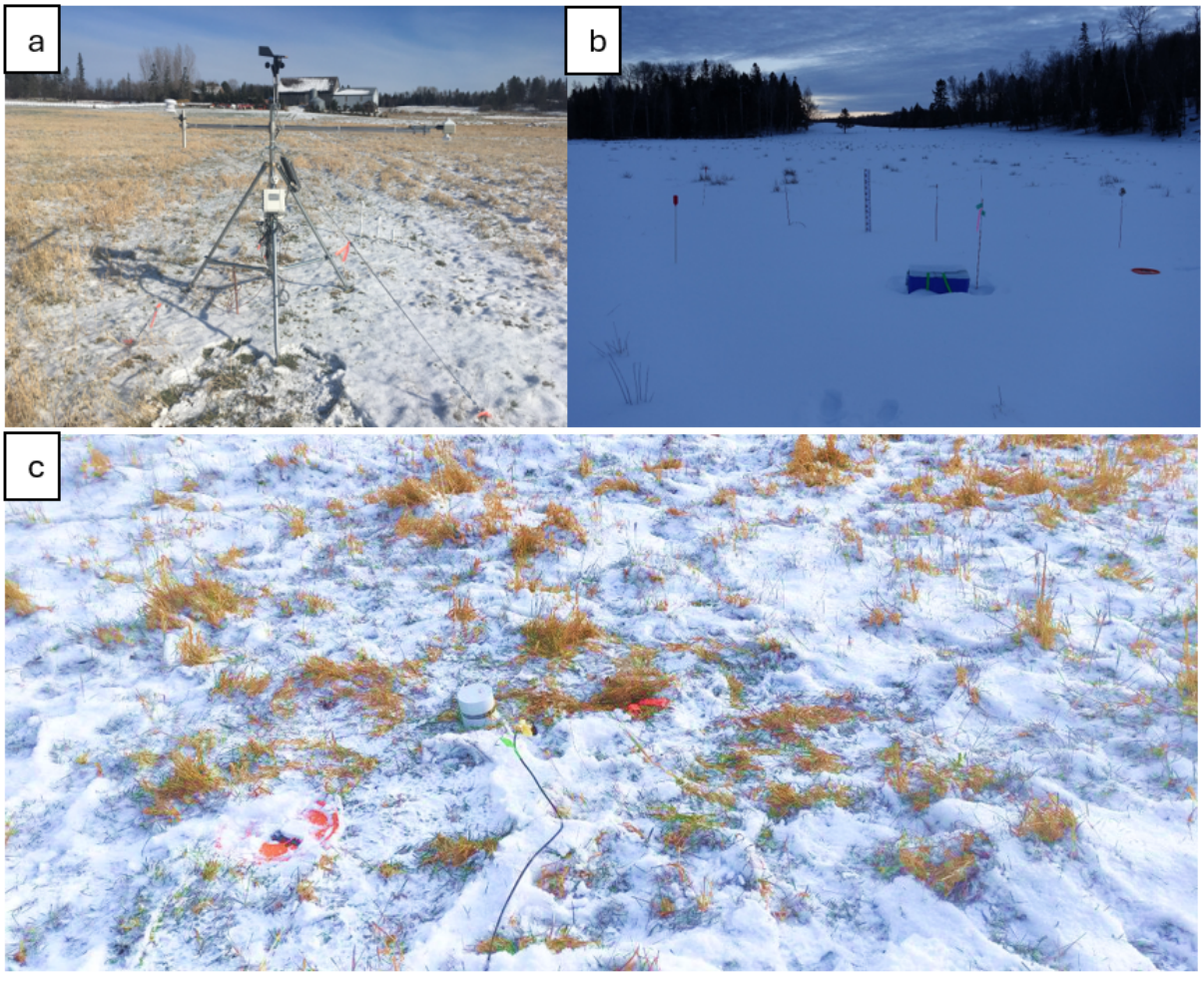

Figure 4. Field instrumentation at the study site. (a) the HOBO weather station used for continuous meteorological measurements. (b) the soil monitoring station, and (c) a soil sensor installed vertically at a depth of 5.7 cm for subsurface relative permittivity and temperature measurements.

Precipitation events were noted using the Environment and Climate Change Canada (ECCC) from the North Bay airport (YYB) weather station (46.37°N, 79.40°W), for all SAR acquisition dates Table 4 was expected to fall as rain, as inferred from the daily minimum and maximum temperatures (Environment and Climate Change Canada, 2024). During the period of missing weather station observations, air temperature and snow depth data from the North Bay ECCC station were used to gap fill and are denoted by dashed lines in the time-series plots. Table 4 summarizes total daily precipitation and minimum and maximum daily temperatures recorded by the ECCC weather station that coincided with the SAR acquisition. For these dates, hourly precipitation data, particularly during the morning and early afternoon hours, were analyzed to determine the timing and intensity of rain events. Dates marked with (*) indicate instances where a decrease in snow on the ground was observed in the hourly records, which we attribute to melting caused by rainfall.

https://doi.org/10.5194/egusphere-2026-1065
Preprint. Discussion started: 7 April 2026

Table 4. Total daily precipitation and minimum and maximum daily temperatures recorded by the ECCC weather station

Date	Max Temperature (°C)	Min Temperature (°C)	Precipitation (mm)
2022-12-30*	7	1.8	1.1
2023-02-14	4.4	-12.3	0
2023-02-15*	4.8	-2.6	16.9
2023-03-17	4	-6.5	10
2023-11-13*	5.6	-0.2	3.1

Dates marked with (*) indicate instances where a decrease in snow on the ground was observed in the hourly records, which we attribute to melting caused by rainfall.

2.4 Polarimetric SAR

SAR polarimetry is a technique that extracts physical information on a target by leveraging its polarization signal characteristics. For our study, it is particularly valuable to investigate soil F/T processes beneath the snow layer. Fully polarimetric SAR systems record complex scattering values in four polarization channels: $S_{HH}, S_{HV}, S_{VH}, S_{VV}$ (Hänsch et al., 2020). Polarimetric target decomposition enables the interpretation of scattering characteristics by analyzing the polarimetric response at a given frequency and imaging geometry (Akhavan et al., 2021; Hajnsek and Desnos, 2021). This technique is generally categorized into two types: coherent and incoherent (Hajnsek and Desnos, 2021). Coherent decomposition relies directly on the scattering matrix and is suitable for isolated, deterministic targets exhibiting fully polarized returns. It can be expressed as Eq. (1) (Turkar and Rao, 2011).

$$\mathbf{S} = \begin{bmatrix} S_{\mathrm{HH}} & S_{\mathrm{HV}} \\ S_{\mathrm{VH}} & S_{\mathrm{VV}} \end{bmatrix}, \qquad \text{Reciprocity} : S_{\mathrm{HV}} = S_{\mathrm{VH}} \tag{1}$$

Natural environments, such as snow-covered soils, consist of distributed scatterers that exhibit distinct polarimetric scattering signatures. For such media, the scattering matrix alone is insufficient to characterize the scattering behavior. Instead, second-order statistical descriptors, namely the covariance matrix $[C]$ and the coherency matrix $[T]$, are employed to capture the ensemble average of polarimetric responses, accounting for the spatial and temporal variability and randomness of natural targets (Moreira et al., 2013). A more detailed theoretical and mathematical explanation of these matrices can be found in (Lee and Pottier, 2017).

Second-order decomposition techniques based on these descriptors are typically categorized into model-based and eigenvalue-, eigenvector-based methods (Moreira et al., 2013). Among high-order polarimetric decomposition techniques, the model-based Freeman–Durden three-component decomposition, commonly associated with natural terrain (Freeman and Durden, 2002), is used. This method enables a simplified, yet physically meaningful interpretation of complex backscatter patterns. The technique attempts to represent the average scattering mechanism as a weighted sum of distinct, physically meaningful components, each corresponding to a scattering process (e.g., surface, double-bounce, or volume scattering).

https://doi.org/10.5194/egusphere-2026-1065
Preprint. Discussion started: 7 April 2026

2.5 Improved Integral Equation Model

In snow-covered agricultural regions, polarimetric signatures typically contain contributions from both the snow or vegetation layer and the underlying soil. To retrieve soil parameters accurately, it is essential to first isolate the scattering effects of the snow or vegetation layer. Once the contribution of these layers have been removed, the remaining signal, primarily influenced by soil relative permittivity and surface roughness. To accurately characterize the soil response, the use of physically based scattering models is necessary to separate and quantify the individual scattering contributions from different surface components. Investigating bare soil in the absence of snow or vegetation represents the most straightforward and historically established approach for soil moisture retrieval using SAR observations. In this context, three primary modeling approaches are commonly employed to characterize the SAR backscatter response: empirical, semi-empirical, and theoretical models.

Theoretical models are based on electromagnetic wave theory and aim to characterize radar backscatter as a function of surface roughness and dielectric properties. The Integral Equation Model (IEM) is one such widely used model for retrieving soil moisture in bare to sparsely vegetated areas (Baghdadi et al., 2011; Tao et al., 2017; Zhang et al., 2018). As a physically-based backscattering model, the IEM is applicable under a wide range of surface roughness conditions. Although the full mathematical formulation of the model is complex and beyond the scope of this paper, it is comprehensively described in (Long and Ulaby, 2015; Fung et al., 1992). The IEM solves integral equations for tangential surface fields while accounting for factors such as the incidence angle, the surface root mean square height (RMSH), the autocorrelation function (ACF) of a one-dimensional roughness profile, and the relative permittivity. The Improved Integral Equation Model (I^2EM), employed in this study, is an improved version of the IEM.

Fung et al. established the Improved Integral Equation Model (I^2EM) (Fung et al., 2002) by incorporating a phase factor into the single-scattering component when calculating the average backscattered signal. The I^2EM builds upon the IEM by integrating both small-perturbation and Kirchhoff approximations, thereby enhancing its sensitivity to cross-polarized returns and depolarization effects associated with surface roughness. To integrate surface fields from both the upper and lower media, the phase factor is used. While I^2EM uses similar input parameters, such as surface roughness (RMSH and correlation length), complex relative permittivity (real and imaginary parts), polarization state, incidence angle, and radar frequency, it expands the model's validity across a broader range of surface conditions. This physically-based approach estimates the backscattering coefficient of randomly rough surfaces under various polarization configurations. It is applicable over a wide range of surface roughness conditions (valid for $ks < 3.0$), making it suitable for simulating the backscatter response from natural surfaces (Inoubli et al., 2024; Fung et al., 2002). The mathematical equation of the I^2EM is provided in Eq. (2) and Eq. (3).

$$\sigma_{qp}^{\mathrm{s}} = S(\theta,\theta_{\mathrm{s}})\frac{k^2}{2}\exp\left[-h^2\left(k_z^2+k_{\mathrm{sz}}^2\right)\right] = \sum_{n=1}^{\infty} h^{2n}\left|I_{qp}^n\right|^2\frac{W^{(n)}(k_{\mathrm{sx}}-k_x,k_{\mathrm{sy}}-k_y)}{n!} \tag{2}$$

$$I_{qp}^n = (k_{\mathrm{sz}}+k_z)^n f_{qp}\exp\Big(-h^2k_zk_{\mathrm{sz}}\Big) + \frac{(k_{\mathrm{sz}})^nF_{qp}(-k_x,-k_y)+(k_z)^nF_{qp}(-k_{\mathrm{sx}},-k_{\mathrm{sy}})}{2} \tag{3}$$

https://doi.org/10.5194/egusphere-2026-1065
Preprint. Discussion started: 7 April 2026

In the above expression for the bistatic single scatter surface backscattering coefficient σ^s_{qp}, the parameters are defined as follows. The term $S(\theta, \theta_s)$ represents a bistatic shadowing function. The variable k denotes the wave number. The quantities k_x, k_y, k_z and k_{sx}, k_{sy}, k_{sz} are the vertical components of the incident and scattered wave vectors, respectively. The parameter h represents the rmsh of the surface roughness. The f_{qp} and F_{qp} parameters are the field coefficients related to Fresnel reflectance, and $W^{(n)}$ is the Fourier transform of the nth power of the surface correlation coefficient.

This study uses the model as a forward surface scattering simulator to simulate the backscatter response from the soil surface beneath a snow-covered layer. The primary objective was to evaluate the ability of I^2EM to estimate soil F/T states over an agricultural region using fully polarimetric L-band observations. Additionally, discrepancies between the measured radar backscatter coefficients and those predicted by the model were examined to assess the model's performance under varying surface and subsurface conditions.

2.6 Soil Freeze/Thaw Retrieval

The determination of the soil F/T state is based on analyzing radar backscatter signals to detect temporal variations associated with changes in soil permittivity as it transitions between frozen and thawed conditions. (Derksen et al., 2017) employed the SMAP baseline F/T algorithm, which uses a seasonal threshold approach to evaluate the temporal evolution of remote sensing observations relative to reference signatures representing frozen and thawed states. For active microwave observations, a seasonal scale factor, $\Delta(t)$, is defined for each acquisition at time t as Eq. (4):

$$\Delta(t) = \frac{\sigma(t) - \sigma_{\mathrm{fr}}}{\sigma_{\mathrm{th}} - \sigma_{\mathrm{fr}}} \tag{4}$$

where $\sigma(t)$ denotes the backscatter measurement at time t for which the F/T classification is sought, and σ_{fr} and σ_{th} represent the reference backscatter values for frozen and thawed conditions, respectively. A threshold value T is then applied such that $\Delta(t) > T$ corresponds to thawed conditions, while $\Delta(t) \leq T$ indicates frozen conditions. σ_{fr} and σ_{th} were determined based on the three lowest and three highest ranked σ^0_{VV} values, respectively. The algorithm was applied on a pixel-by-pixel basis. Following the procedure in Eq. (4), and using a threshold T, each pixel was classified as either frozen or thawed (binary classification). A threshold value of 0.5 was adopted throughout the F/T season in this study, with the option for further optimization if required.

3 Results

3.1 Soil Freeze/Thaw Monitoring using In Situ Observations

In the absence of snow and permafrost, the F/T state of the soil profile is primarily driven by air temperature variations. Freezing generally begins when daily air temperatures consistently drop below $0\,^{\circ}\mathrm{C}$, while thawing commences when soil temperatures rise above $0\,^{\circ}\mathrm{C}$. Although air temperature is the dominant control, the presence or absence of snow complicates the timing of these transitions.

https://doi.org/10.5194/egusphere-2026-1065
Preprint. Discussion started: 7 April 2026

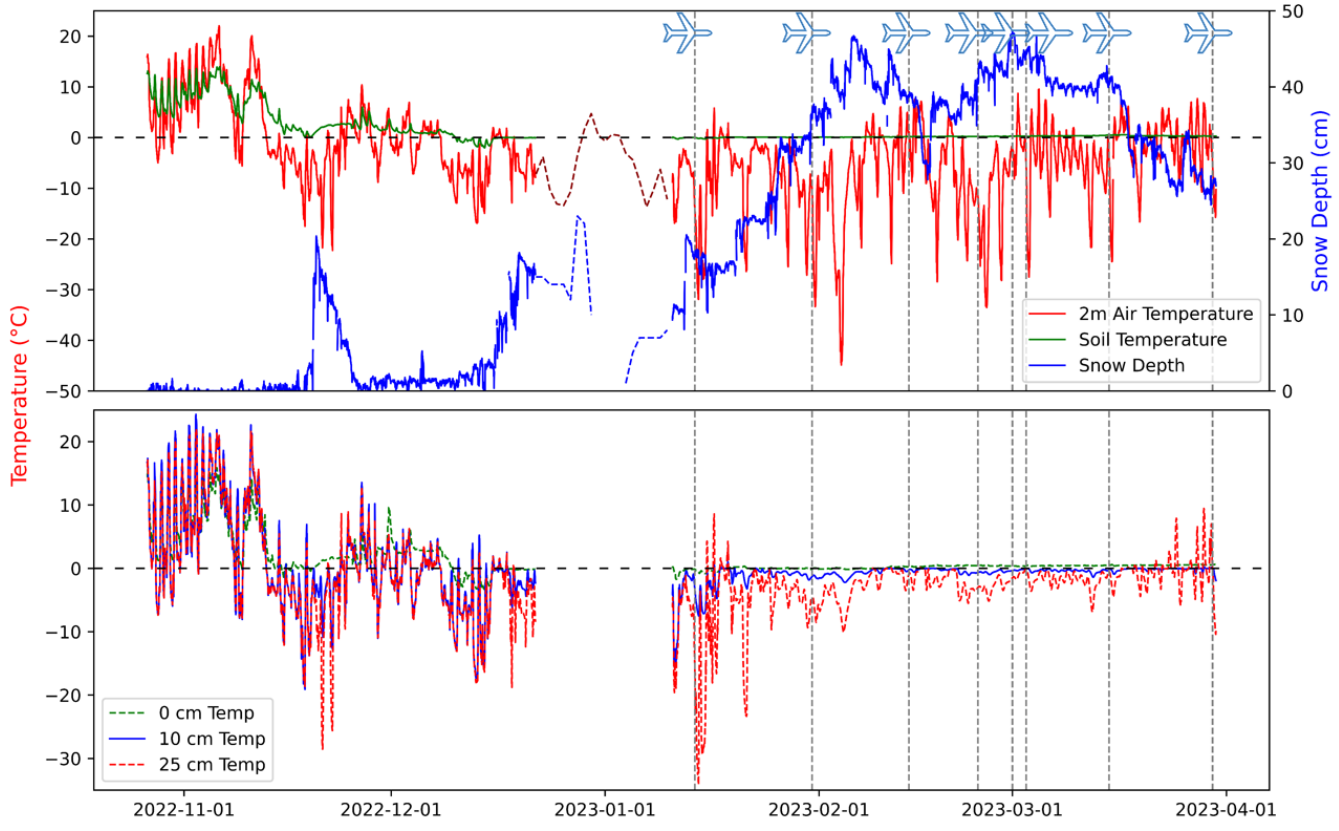

Figure 5. Hourly time series of environmental measurements recorded by the local study area weather station. The top plot shows 2 meter air temperature, soil temperature, and snow depth, illustrating overall temporal variations in air and ground conditions. The bottom plot presents snow temperature measured at three heights just above the ground surface, highlighting the evolution of snowpack temperatures as the snow depth varied throughout the observation period.

As shown in Fig. 5, snow depth ranged from zero to approximately 0.5 m, with a standard deviation of 16.96 cm based on the acoustic Judd snow depth sensor mounted to the local weather station. Snow accumulation in the study area began in late October; however, early snowfall events were intermittent and readily melted in response to daily temperature fluctuations. A more persistent snow layer developed by mid-November, reaching a depth of approximately 20 cm, but gradually decreased toward the end of the month responding to warmer air temperatures. Thereafter, only a shallow snow cover remained, persisting until mid-December. Observations of snow depth across different field locations, using both manual and UAV LiDAR–derived techniques, indicated within-field spatial variability, with deeper accumulations in certain areas. Overall, the temporal evolution of snow depth closely followed the locally measured air-temperature regime of warming and cooling, confirming the strong relationship between atmospheric conditions and snow persistence. In addition to snow depth, the weather station recorded both soil and snow temperatures using thermocouple probes installed at three heights near the ground surface. The probes measured

https://doi.org/10.5194/egusphere-2026-1065
Preprint. Discussion started: 7 April 2026

snow temperatures as the snow deepened and buried them, and air temperatures when the snow was absent or shallow, all serving as key indicators for identifying soil F/T states.

In this study, frozen/thawed classification was based on combined soil temperature and real permittivity thresholds. Although the imaginary part of permittivity influences the characterization of thawed soils, the analysis here focuses on the real part, given that the field campaign mainly captured frozen conditions. The temperature criterion classified soil as frozen when $\leq 0\,^{\circ}\mathrm{C}$ and thawed when $> 0\,^{\circ}\mathrm{C}$. The permittivity criterion classified soil as frozen when $\epsilon' < 10$ and thawed when $\epsilon' \geq 10$. The combined classification assigned a frozen state when both temperature $\leq 0\,^{\circ}\mathrm{C}$ and $\epsilon' < 10$, and a thawed state when temperature $> 0\,^{\circ}\mathrm{C}$ and $\epsilon' \geq 10$. This approach reduced false detections caused by temperature sensor noise or permittivity variability. Transparent blue and red epochs in Fig. 6 indicate frozen and thawed soil states, respectively.

https://doi.org/10.5194/egusphere-2026-1065
Preprint. Discussion started: 7 April 2026

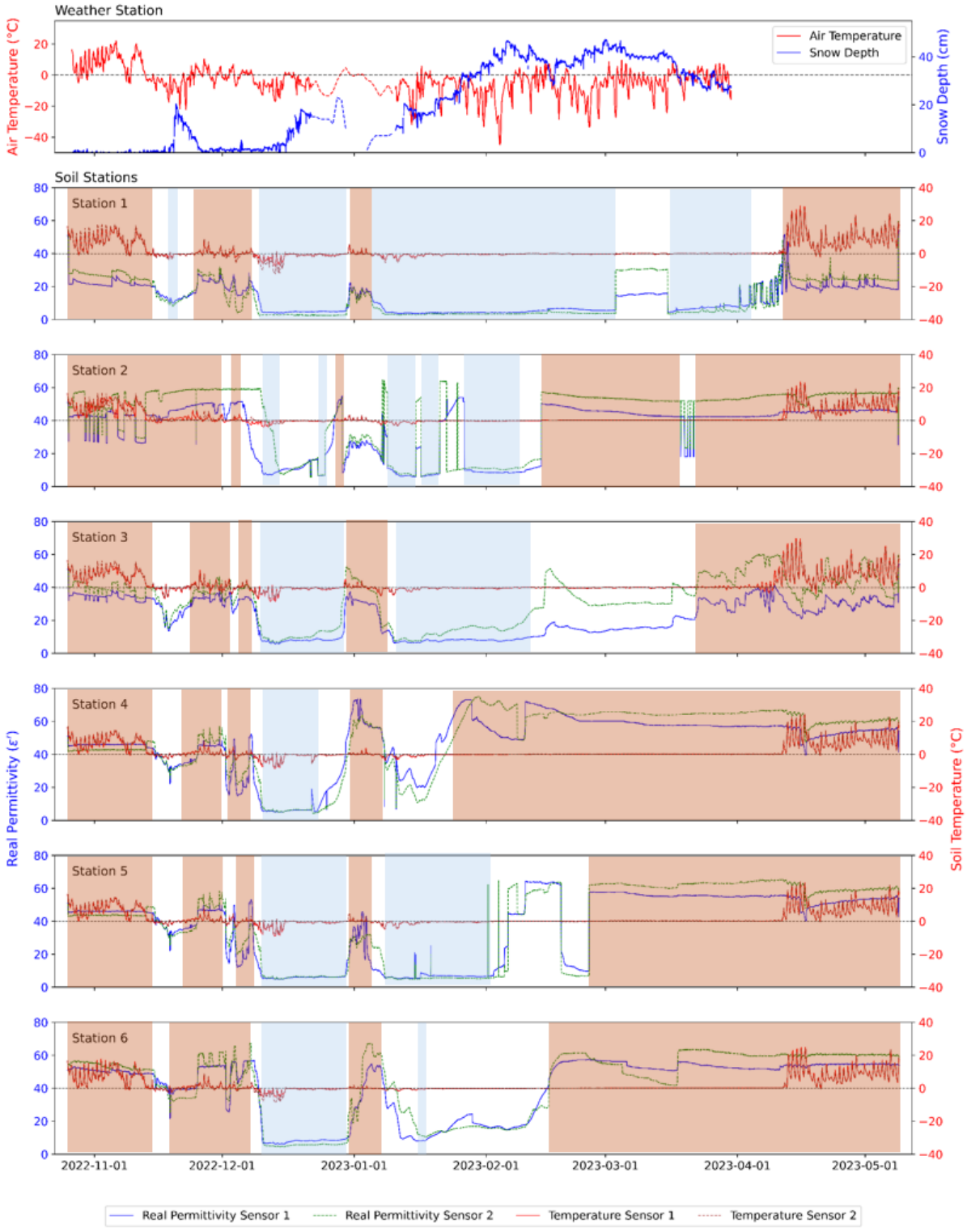

Figure 6. Time series of soil measurements recorded by the Steven Hydra Probes. The plot shows soil relative permittivity (ϵ') alongside soil temperature (°C), illustrating temporal variations in soil dielectric properties and thermal conditions at the measurement site.

https://doi.org/10.5194/egusphere-2026-1065
Preprint. Discussion started: 7 April 2026

Soil moisture and temperature data were collected from a network of soil monitoring stations representing different vegetation conditions, grazing stages, and elevations across the study domain. These soil stations were named to assist local surveyors with identification and data management. The names chosen were related to the crop types present and/or their physical locations. The soil stations Winter Rye, Central, and Lower (installed 15 November 2022) recorded data without interruption for the entire 2022-2023 winter season. The Eastern soil station recorded from 10 November 2022 to 15 December 2022; the Upper station experienced frequent interruptions between 12 December 2022 and 14 February 2023; and the East Dry station (installed 1 December 2022) had multiple interruptions between 30 January 2023 and 15 February 2023 and stopped recording from 28 February 2023 onward. Some data gaps, particularly for the East Dry time series, occurred when the ground was frozen, making the extraction and replacement not possible. Missing soil temperature values were filled using Inverse Distance Weighting (IDW), with available measurements from other stations at the same timestamp weighted by the inverse square of their geographic distance, ensuring temporal continuity for analysis.

According to the soil monitoring network of Stevens HydraProbes, soils were predominantly thawed at all stations from the 2022 mid-November installation date until early December 2022. Soil temperature first dropped below $0\,^{\circ}\mathrm{C}$ in early December, concurrent with a sharp decrease in ϵ', and remained low until late December. At the beginning of January, both soil temperature and ϵ' increased. Although the local weather station was not recording during this period, interpolated values from nearby stations confirmed a rise in air temperature and a reduction in snow depth. Based on minimum/maximum air temperature and hourly precipitation data from the nearby ECCC station (Table 4), rainfall also contributed to soil thawing, a reduction in snow depth, and an increase in infiltration of moisture into the underlying soil. From mid-January onwards, most soil stations showed strongly consistent conditions except at the Lower and Winter Rye soil stations. The East Dry soil station began recording erroneous values for a few days in January before failing completely at the end of the month; thus, IDW-interpolated values for this period may be unreliable.

In mid-February 2023, the nearby ECCC North Bay weather station (Table 4) measured air temperatures above $0\,^{\circ}\mathrm{C}$ and precipitation as rain, concurrent with an increase in the local on-site weather station's air temperature and a decrease in local station's snow depth. Although mean soil temperatures recorded by the local soil monitoring network appeared constant ($\approx 0\,^{\circ}\mathrm{C}$) from mid-January 2023 to season's end in April 2023, a zoom-in plot (Fig. A1), revealed fluctuations between slightly negative and positive values, suggesting the snow layer acted as an insulator for the underlying soil, muting the intensities of the melt events, but not fully preventing several F/T transitions. Snow temperatures (Fig. 5) showed increasing temperatures from the snow surface toward the soil interface, highlighting that the soil was warmer than the air. Despite persistent snow cover until the end of the campaign in April 2023, the local weather station within the study domain intermittently recorded above ($0\,^{\circ}\mathrm{C}$ snow and air temperatures, coincidentally with the soil stations recording high ϵ' values, indicating a dominant thawed state after early March 2023, except at the Central soil station, where soils recorded consistently frozen from mid-March to early April.

https://doi.org/10.5194/egusphere-2026-1065
Preprint. Discussion started: 7 April 2026

3.2 Variability and Magnitude of L-band VV Backscatter

This section investigates the variability of soil F/T state using VV polarization, as VV polarization is strongly influenced by soil dielectric changes and provides a reliable indicator of F/T transitions. Cross-polarized channels showed less consistent variation, underscoring VV's sensitivity to dielectric changes. The analysis focuses on characterizing both the magnitude (low vs. high backscatter) and the spatial variability (low vs. high field variability) of VV response, while the full temporal evolution is provided in Appendix (Fig. A2). VV backscatter is particularly sensitive to soil F/T changes because it penetrates the snow layer with minimal attenuation, while being less affected by vegetation (≤ 20 cm, stable during the campaign) and roughness compared to cross-polarization. Considering the co-polarized response, VV generally exhibits stronger sensitivity to soil permittivity changes than HH, particularly at higher incidence angles (Zeng and Chen). In contrast, HH tends to show slightly greater sensitivity to variations in surface roughness compared to VV (Holah et al., 2005; Singh et al., 2023). Thus, VV provides a clearer signal of soil dielectric transitions. As expected, frozen soils with reduced dielectric constant are associated with low backscatter, whereas thawed soils exhibit higher backscatter driven primarily by soil moisture content. This confirms that VV backscatter is a reliable proxy for detecting soil dielectric state under snow-covered agricultural region compared to cross-polarization channel.

Examples of these states were observed in the field. On 12 January 2024, all stations showed a pronounced low backscatter response, consistent with fully frozen soil conditions. In contrast, 1 March 2024 exhibited a high backscatter response, coinciding with thaw conditions, an increase in 2 meter air temperature, and higher soil permittivity across all stations (Fig. 6). These examples illustrate how VV backscatter distinctly separates frozen from thawed soil states, even under dry snow cover. Soil state transitions were not uniform across all field sites on all dates. On 14 January 2023, backscatter exhibited high spatial variability, indicating that different field sections transitioned at different times depending on local parameters (e.g., soil type, moisture). Conversely, on 15 March 2024, spatial variability was relatively low, suggesting more uniform surface conditions. This contrast highlights that spatial heterogeneity in F/T timing is an intrinsic feature of agricultural landscapes, and that L-band VV backscatter can capture both homogeneous and heterogeneous transitions across the field.

While dry snow at L-band contributes minimally to total backscatter, it modulates the soil signal through direct backscatter and attenuation. Nevertheless, as shown in (Fig. 6), the long wavelength of L-band allowed penetration through the snow layer, making soil-related transitions the dominant signal. This reinforces the robustness of L-band VV for F/T monitoring in snow-dominated environments, where shorter wavelengths may fail. Field boundaries and roughness differences were also clearly visible, further demonstrating the insensitivity of L-band backscatter to dry snow cover.

https://doi.org/10.5194/egusphere-2026-1065
Preprint. Discussion started: 7 April 2026

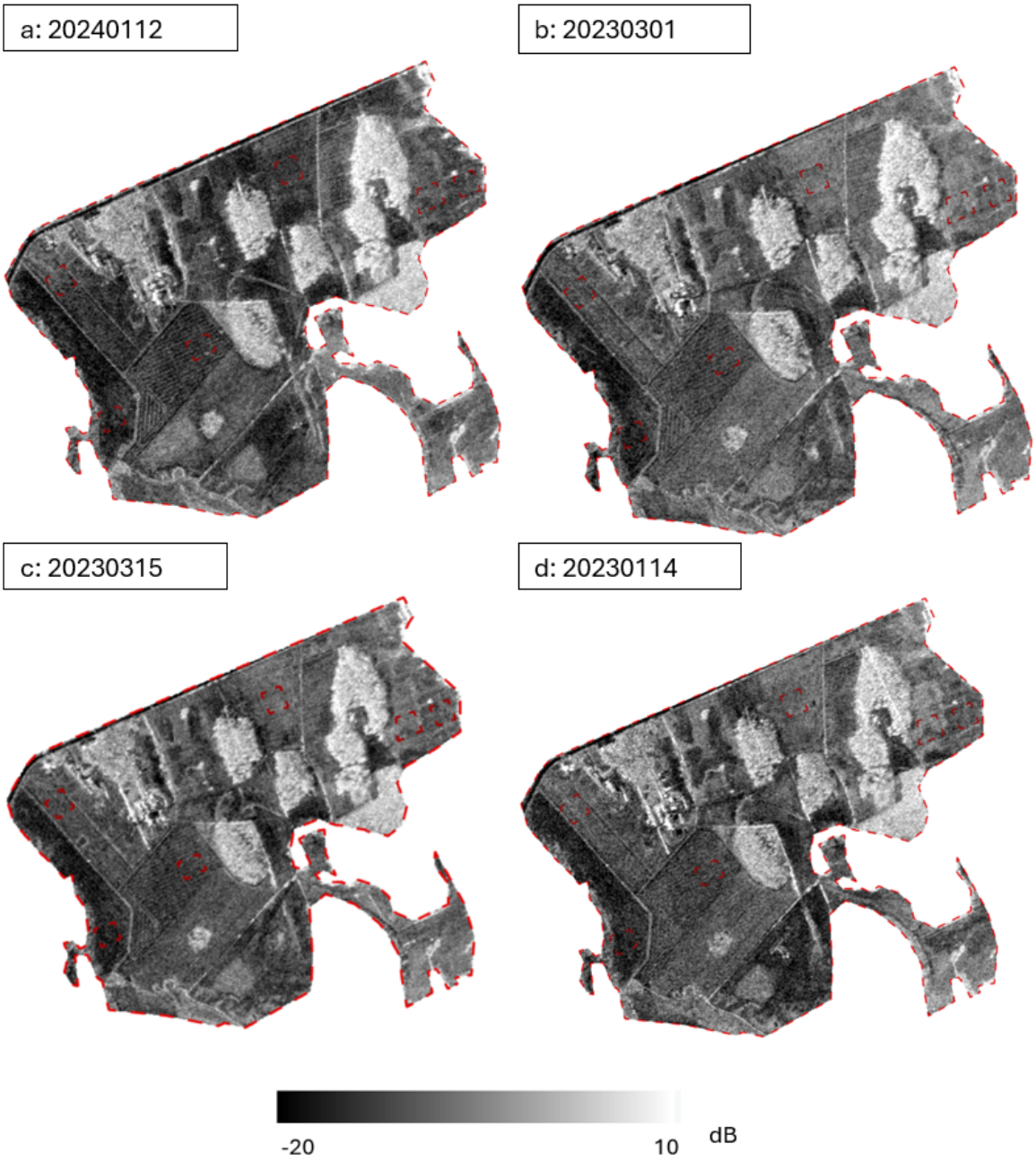

Figure 7. Spatial distribution of σ^0_{VV} across the CryoSAR field site, illustrating (a) low backscatter, (b) high backscatter, (c) low spatial variability, and (d) high spatial variability.

The temporal evolution of mean σ^0_{VV} values, averaged within soil moisture regions of interest for each station (± 1 std), is presented in Fig. 7. From mid- to late January, a consistent increase in backscatter was observed across stations, with

https://doi.org/10.5194/egusphere-2026-1065
Preprint. Discussion started: 7 April 2026

the largest rises of +1.56 dB at Winter Rye and +1.52 dB at Upper, while East Dry remained relatively stable (+0.62 dB). This increase coincided with rising 2 meter air temperature, a reduction in snow depth, and warming of the snowpack layers (Fig. 7). Following this period, backscatter stabilized or decreased slightly: between late January and mid-February, most stations showed only minor changes, with Winter Rye decreasing by -0.62 dB and Eastern remaining stable. From mid- to late February, stations exhibited mixed trends, with decreases at Central, East Dry, and Eastern, which aligned with soil and weather station records (Fig. 5 and Fig. 6).

The winter of 2023–24 displayed unique characteristics compared to typical mid-latitude Canadian winters. November 2023 did not experience persistent cold conditions, resulting in an unusually high backscatter response, which confirmed that soil remained unfrozen. In contrast, mid-January was marked by very shallow or absent snow cover. The thin snow layer did not insulate the soil from the cold air temperature, driving a rapid soil freeze and producing a sharp decrease in backscatter across all stations. Together, these temporal patterns demonstrate that while backscatter broadly tracks temperature-driven F/T transitions, local soil and microclimatic differences control the exact timing and magnitude of response.

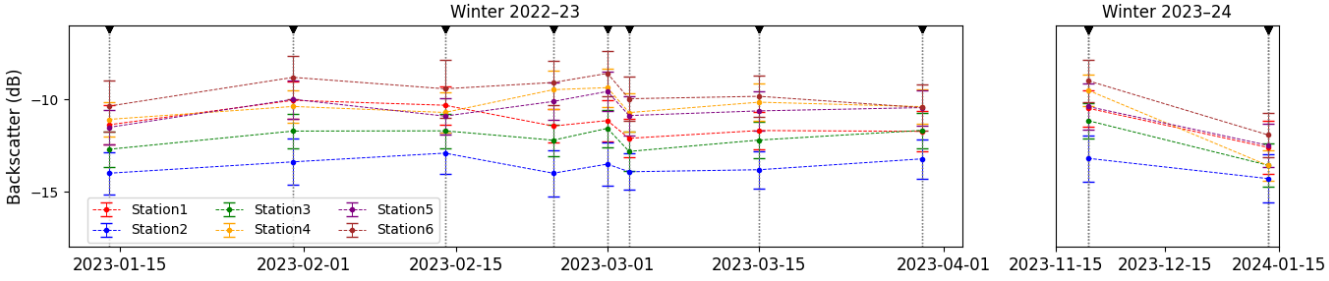

Figure 8. Temporal evolution of the VV backscatter response measured over six soil stations during the CryoSAR field campaign. The plot shows the mean VV backscatter with ±1 standard deviation throughout winter 2023 and winter 2024, illustrating spatial and temporal variations across the study area.

3.3 Changes in Polarimetric Decomposition Parameters

Changes in relative permittivity of the soil help us identify F/T state of the soil using the polarimetric SAR information. The high penetration depth of L-band SAR limits sensitivity to short stubble (mostly ≤ 20 cm) present in the field. This penetration capability also reduces dihedral scattering between vegetation stalks and underlying soil. Consequently, this section focuses only on the evolution of surface and volume scattering.

Figure 8 illustrates the low and high surface scattering responses, as well as the spatial variability of surface scattering response across the field. The lowest surface scattering response occurred in late January, reaching -16.28 dB at the East Dry station. During this period, all fields were frozen, as confirmed by real permittivity values measured by soil sensors (Fig. 6) and by the 2 meter air temperature recorded at the ECCC weather station, which dropped to -30 (Fig. 5). In addition, snow profile temperatures were consistently below freezing, indicating dry snow conditions that enabled the L-band signal to penetrate

https://doi.org/10.5194/egusphere-2026-1065
Preprint. Discussion started: 7 April 2026

the snow layer and interact with the ground. By mid-February, all soil stations except the Central station recorded high real permittivity values, indicating that the soil had transitioned to a thawed state (Fig. 6).

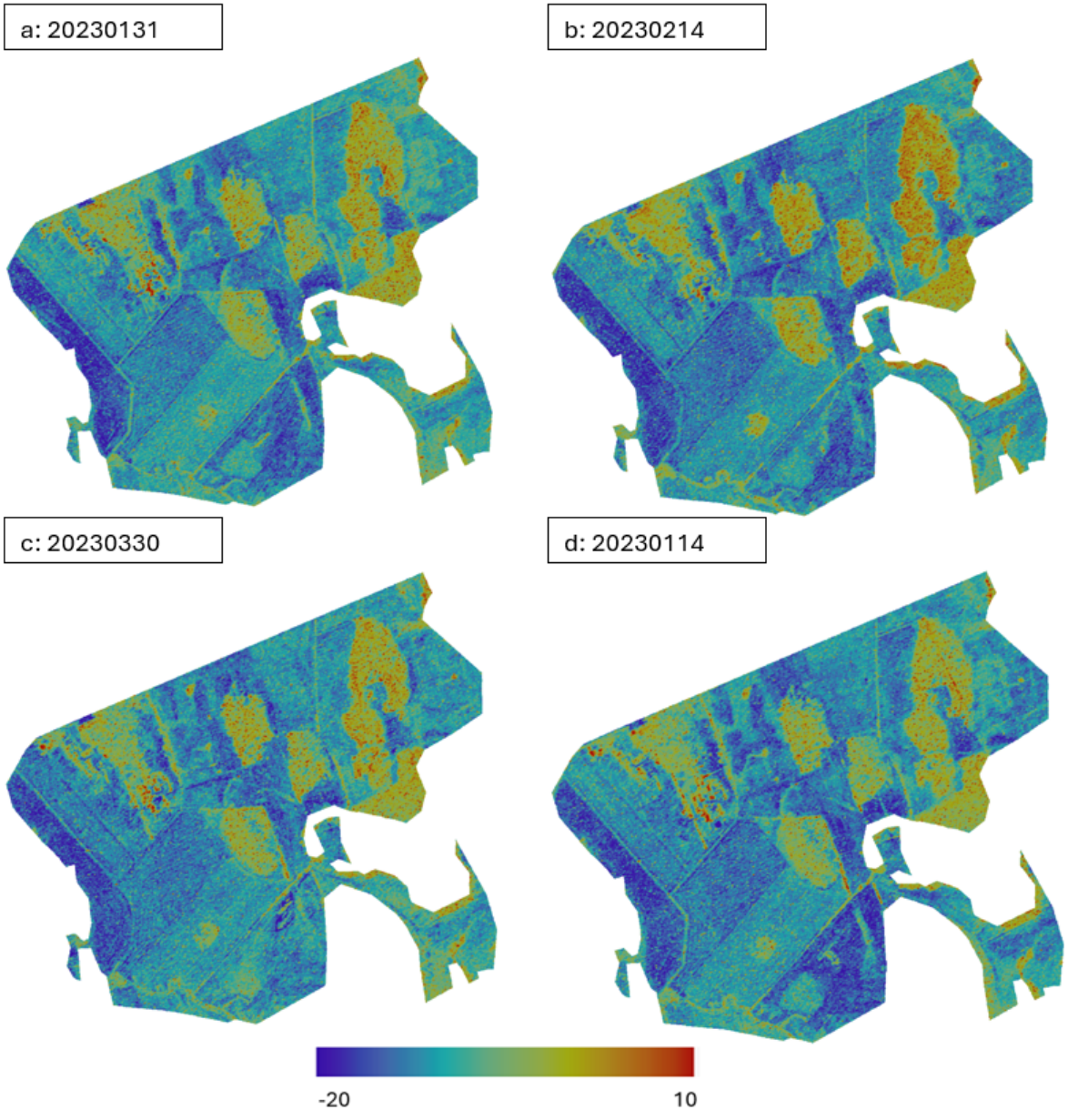

Figure 9. Spatial distribution of surface scattering response across the CryoSAR field site, illustrating (a) low, (b) high, (c) low spatial variability, and (d) high spatial variability of surface scattering component from the model-based Freeman-Durden decomposition.

340 As the soil began to thaw, higher soil moisture levels caused an increase in surface-like scattering, most likely originating from the snow surface rather than the underlying soil. Accordingly, in mid-February the study region experienced a higher

https://doi.org/10.5194/egusphere-2026-1065
Preprint. Discussion started: 7 April 2026

surface scattering response. This increase coincided with positive temperature values recorded by the ECCC weather station. Positive snow profile temperatures, together with 2 meter air temperatures above freezing, further confirm the likelihood of surface scattering from the snow layer. By the end of March 2023, surface-like scattering remained stable and nearly identical across all soil stations. This stability was accompanied by an increase in soil relative permittivity (Fig. 6), positive soil temperatures recorded by all soil sensors (Fig. A1), and positive air temperatures concurrent with a decrease in snow depth observed at the ECCC weather station. Together, these observations suggest the onset of the snowmelt season, during which all stations approached a nearly uniform state.

At the beginning of the airborne campaign in mid-January 2023, the highest variability in surface scattering was observed across soil stations, despite the scattering magnitudes being relatively high at all sites. The positive air temperature recorded at the North Bay weather station, along with 16.9 mm of rainfall (Table 4), likely contributed to the elevated scattering response. In addition, the field was covered by less than 20 cm of shallow snow, which varied across stations. This spatial heterogeneity in snow cover likely led to the observed variability in surface scattering among stations.

Lower frequencies such as L-band SAR are not sensitive to small particles like snow grains. Therefore, under dry conditions, little to no volume scattering contribution is expected from the snow layer. As shown in Fig. 11, after mid-February surface scattering decreased slightly, while volume scattering increased more sharply across all stations. The maximum volume scattering response during the field campaign occurred on March 3. Although air temperature at the ECCC weather station was recorded near -30 (Fig. 5), strong oscillations in temperature during the preceding days led to repeated melt–refreeze events. Field crews also reported the presence of ice layers within the snowpack. These ice layers, together with increased snowpack moisture, likely caused multiple scattering within the snow, thereby enhancing the volume scattering response observed on March 3.

On March 1, positive air temperatures, decreasing snow depth, and near-zero to positive snow profile temperatures (Fig. 5) coincided with the highest variability in volume scattering across the study region. This variability was driven by differences in local microclimatic conditions, field orientation relative to the sun, and snow cover heterogeneity. For example, the East Dry station contained stubble that produced uneven snow accumulation, contributing to the large variability in volume scattering captured by the Freeman–Durden decomposition. On the other hand, the lowest volume scattering response was observed in mid-March across the field (Fig. 10 and Fig. 11). This reduction in volume scattering was consistent with an increase in surface scattering across all stations. At the same time, the 2 meter air temperature dropped below -20, indicating dry snow conditions that explain the reduced volume scattering observed at all soil stations.

https://doi.org/10.5194/egusphere-2026-1065
Preprint. Discussion started: 7 April 2026

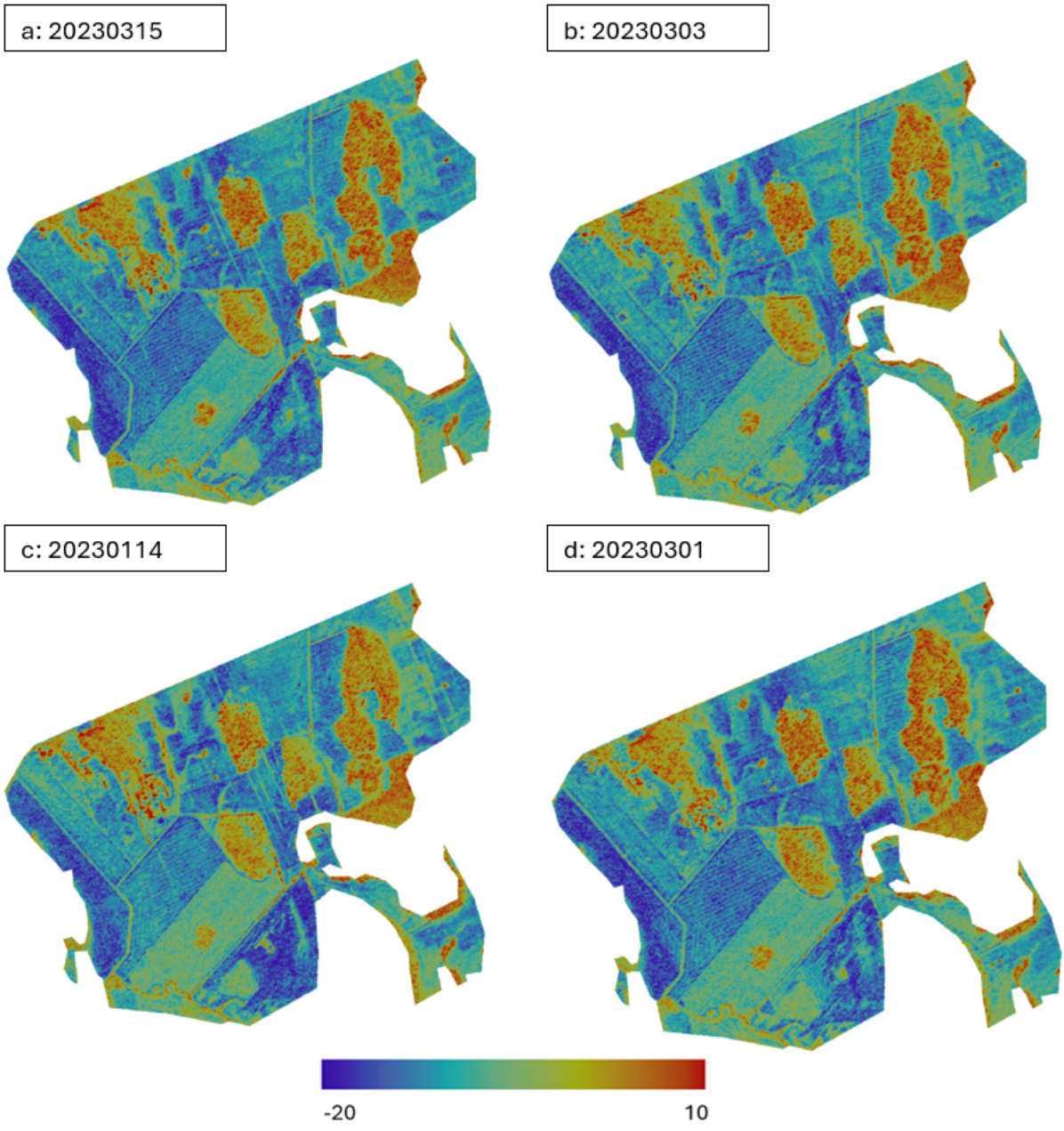

Figure 10. Spatial distribution of volume scattering response across the CryoSAR field site, illustrating (a) low, (b) high, (c) low spatial variability, and (d) high spatial variability of surface scattering component from the model-based Freeman-Durden decomposition.

370 The highest stability across the field was observed at the beginning of the airborne campaign in mid-January. During this period, the 2 meter air temperature was below -30 (Fig. 5), and soil permittivity values (Fig. 6) at nearly all stations were as low as expected for frozen conditions. Figure 11 indicates greater variability in volume scattering compared to surface scattering

https://doi.org/10.5194/egusphere-2026-1065
Preprint. Discussion started: 7 April 2026

throughout the season. As noted by (Wang et al., 2017), the Freeman–Durden decomposition tends to overestimate volume scattering because it does not account for depolarization caused by surface roughness and azimuthal tilt. The volume scattering component, derived from cross-polarized signals, generally decreased under frozen conditions; however, elevated responses were observed on January 31, February 24, and in early March.

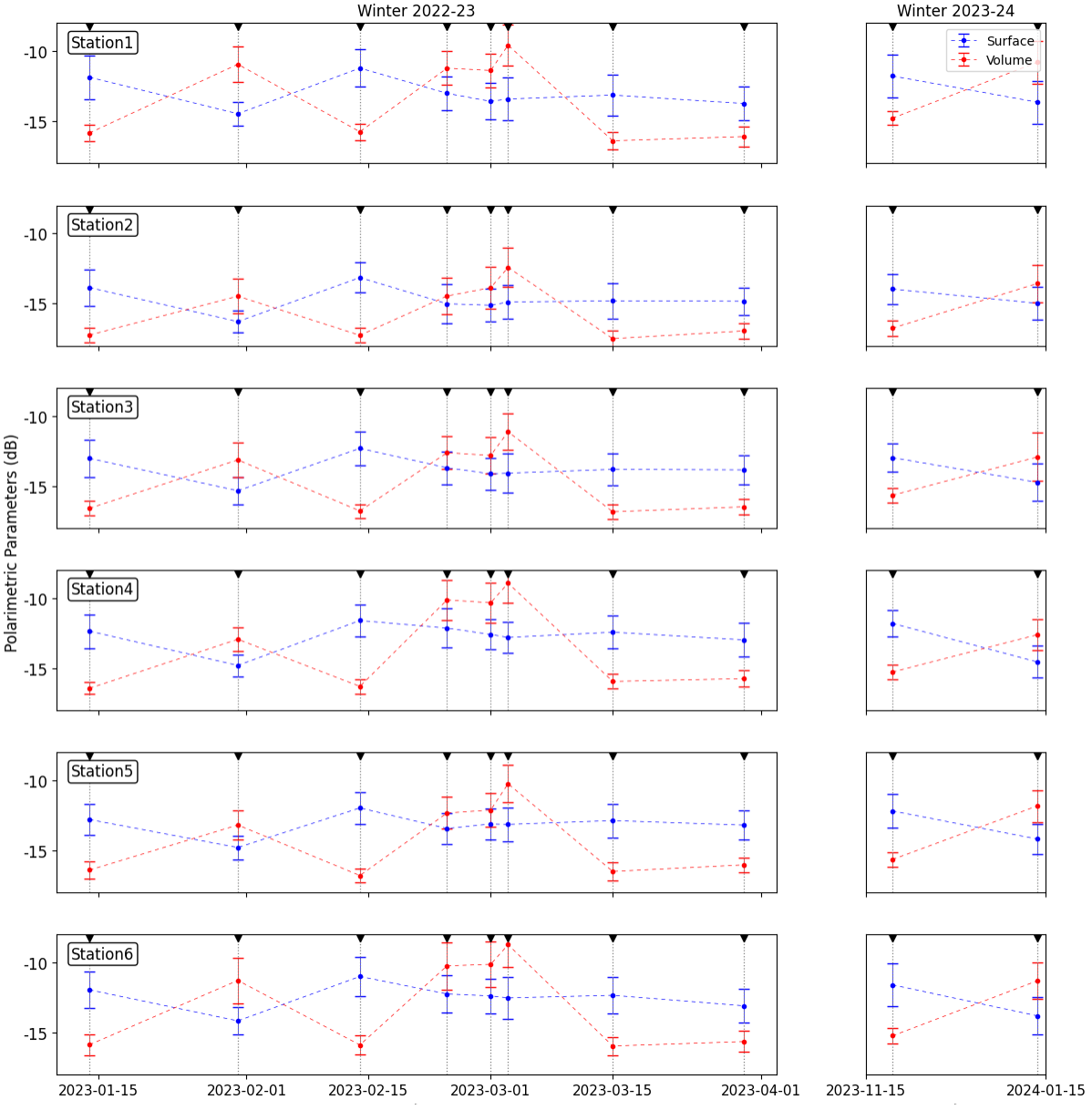

Figure 11. Temporal evolution of polarimetric scattering observed during the CryoSAR field campaign. The plot shows (a) surface scattering and (b) volume scattering, with mean values and ±1 standard deviation, illustrating changes in scattering mechanisms over the study period.

https://doi.org/10.5194/egusphere-2026-1065
Preprint. Discussion started: 7 April 2026

In November 2023, the absence or shallowness of snow cover meant no insulating effect, allowing soil to freeze rapidly and remain frozen. This led to consistently high surface scattering across all stations. Low volume scattering during this period further demonstrates the insensitivity of L-band SAR to short stubble cover, resulting in minimal volume response from vegetation coverage. Winter 2024 exhibited unique characteristics and was considered anomalously warm. Snow cover in winter 2023 acted as an insulator, insulating the soil and preventing heat loss, which led to a decline in surface scattering, clearly evident in Fig. 11. Although statistical values were retrieved from the same region, only three soil stations were installed during the second year, and real permittivity and temperature datasets from these stations were not included here.

3.4 Improved Integral Equation Model

In order to meet the necessity of accurate soil F/T estimation, I^2EM was used as a forward model to simulate microwave signatures and the result is demonstrated in Fig. 12. To evaluate the I^2EM's simulation result, in this experiment, we compared the measured backscattering coefficient from 2023 winter season CryoSAR dataset with simulated backscattering coefficient from I^2EM model.

To simulate the backscattering coefficient in both co- and cross-polarization channels, the I^2EM model was parameterized using the complex relative permittivity at L-band, simulated with the Dobson (1985) dielectric mixing model (Dobson et al., 2007), along with surface roughness parameters (RMS height and correlation length), the incidence angle, and the signal frequency. Among the three correlation functions tested (exponential, gaussian, and x-power), the exponential function provided the best agreement and was therefore used as the correlation function in this study. For soil roughness characterization, UAV-based LiDAR data were collected at an altitude of 30 meter with 1400 points per meter squared over the field site. The 2023–2024 season was not considered in this study due to a change in the soil station measurement strategy.

While physically based models such as I^2EM are mathematically sophisticated compared to empirical soil models and impose a greater computational burden, they offer the advantage of being site-independent. Overall, a reasonable agreement was observed between the modeled and simulated VV and HV backscatter response for most of the fields, with RMSE values of approximately ± 3 dB. However, as noted in previous studies on the IEM (Zribi et al., 2011), the model frequently over- and underestimates the SAR signal depending on the input parameters. The I^2EM model underestimates the SAR signal by more than 9 dB in HH polarization, with a significant difference compared to HV and VV polarizations. In HV polarization, slight over and underestimation is observed, except for the lower and upper stations, where higher underestimation greater than 6 dB occurs. The model simulates the backscattering coefficient at VV polarization with differences between SAR-measured and predicted responses ranging from -3 to 5 dB, and RMSE values between 2.24 and 5.22 dB.

https://doi.org/10.5194/egusphere-2026-1065
Preprint. Discussion started: 7 April 2026

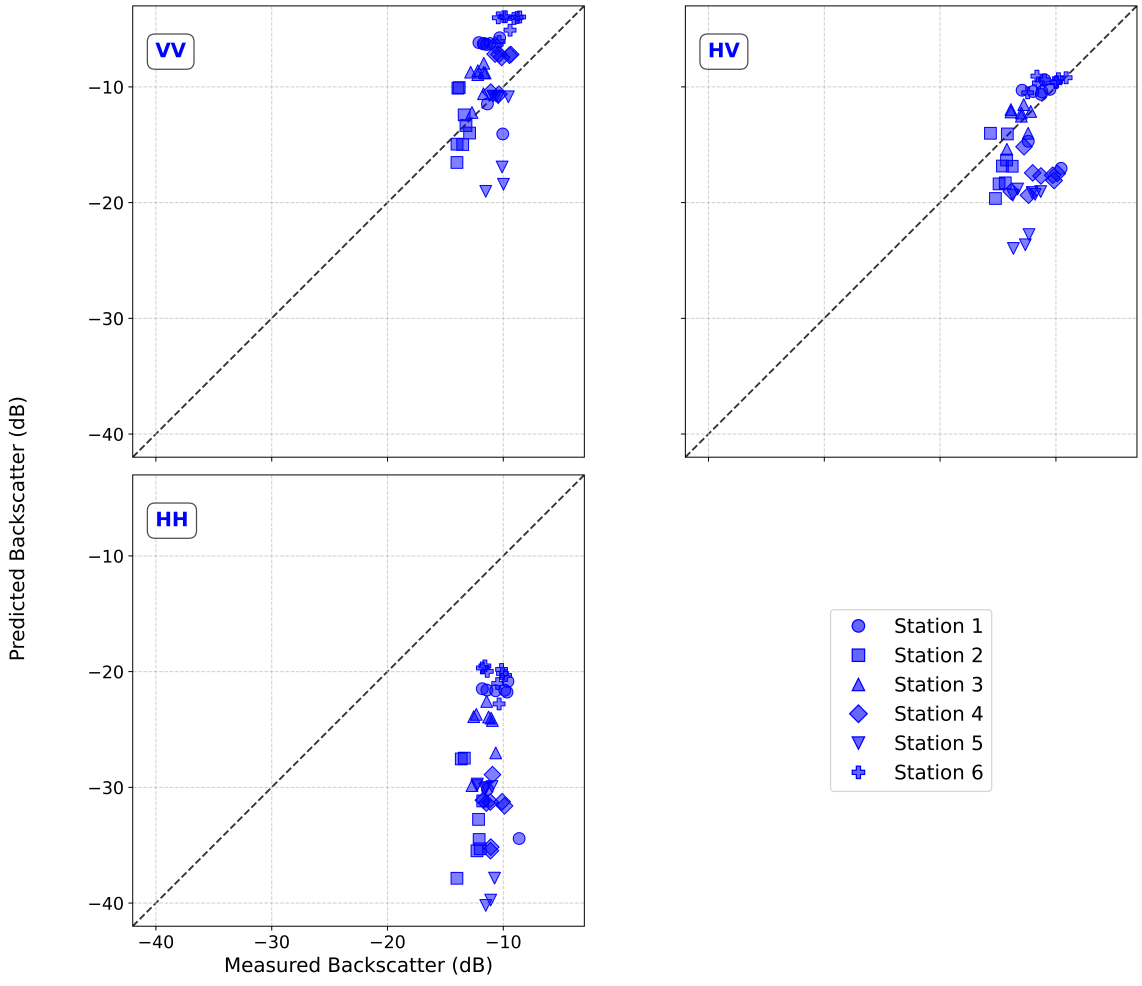

Figure 12. Backscatter response predicted by the I^{2}EM model and measured by L-band SAR.

Since the field campaign took place during the winter months and soil temperatures were slightly below 0, it is reasonable to assume that surface roughness remained largely unchanged throughout the season. Consequently, the seasonal variability of σ^0 is primarily driven by changes in the dielectric properties, whereas the sensitivity to roughness is assessed around a fixed roughness state. Although relative permittivity varied over the season, the I^{2}EM simulations were parameterized using permittivity values simulated by the Dobson (1985) dielectric model based on a single-date gravimetric soil measurement acquired prior to the snow-on season. This assumption introduces uncertainty, as soil permittivity evolved during the field campaign, as demonstrated in Fig. 6.

There is generally better agreement between the backscatter predicted by the I^{2}EM model and the observed CryoSAR L-band backscatter across all six stations for the VV and HV channels compared to the HH polarization, as shown in Table 5 and Fig. 12. RMSE values range from 1.26 to 22.46 dB, with HH polarization showing higher errors at all stations. The HH

https://doi.org/10.5194/egusphere-2026-1065
Preprint. Discussion started: 7 April 2026

polarization consistently demonstrates worser agreement, with RMSE values above 9 dB at all stations. The largest RMSE of 22.46 dB occurs at Station 5 for HH polarization, potentially due to surface roughness or vegetation structure not fully captured by the model input. The VV and HV polarizations exhibit lower error, with RMSE values ranging from 1.26 to 8.40 dB compared to HH.

Table 5. RMSE and bias (dB) values for each station and polarization

Polarization	Statistics	Station 1	Station 2	Station 3	Station 4	Station 5	Station 6
VV	RMSE (dB)	4.76	2.24	3.00	2.70	4.68	5.22
	Bias (dB)	3.40	0.29	2.75	2.31	-3.07	5.16
HV	RMSE (dB)	3.04	2.92	1.26	6.39	8.40	1.45
	Bias (dB)	0.29	-2.17	0.41	-6.16	-8.15	1.13
HH	RMSE (dB)	14.77	20.46	13.45	21.19	22.46	9.81
	Bias (dB)	-13.81	-20.10	-13.28	-21.09	-21.93	-9.70

Stations exhibiting particularly large errors reflect higher temporal variability in the observed backscatter or increased model uncertainty arising from local factors such as residual vegetation cover and spatial heterogeneity in soil moisture and surface roughness. The simulated backscattering coefficients systematically deviate from the 1:1 line, indicating a mismatch in slope between I^2EM-predicted and CryoSAR-observed values. This discrepancy is most pronounced in the HH channel, where the model generally underestimates the backscatter magnitude, indicating limited capability of I^2EM in simulating L-band backscatter. Such polarization-dependent behavior suggests that model performance is strongly influenced by the accuracy of the gravimetric soil input and surface roughness parameterization, and that the model sensitivity to dielectric and roughness inputs is not fully captured under transitional F/T conditions.

3.5 CryoSAR-derived Freeze/Thaw Maps

Examples of F/T maps derived from CryoSAR L-band data using the approach described in Section 2.6 are presented in Fig. 13. For comparison, F/T maps corresponding to the same date as Fig. 7 are shown to evaluate the performance of the classification algorithm.

Although the study region was relatively small and homogeneous, the F/T maps captured the frozen and thawed soil states within an acceptable range. Across multiple dates, the algorithm performed better on the western side of the field, while the eastern side was predominantly classified as thawed. Vegetated regions were masked (can be seen as white) using ESA World Cover 2021 in Google Earth Engine. No reference or in situ data were available to validate the tree-covered areas. Therefore, wooded regions were masked (appearing in white) using ESA World Cover 2021 in Google Earth Engine.

https://doi.org/10.5194/egusphere-2026-1065
Preprint. Discussion started: 7 April 2026

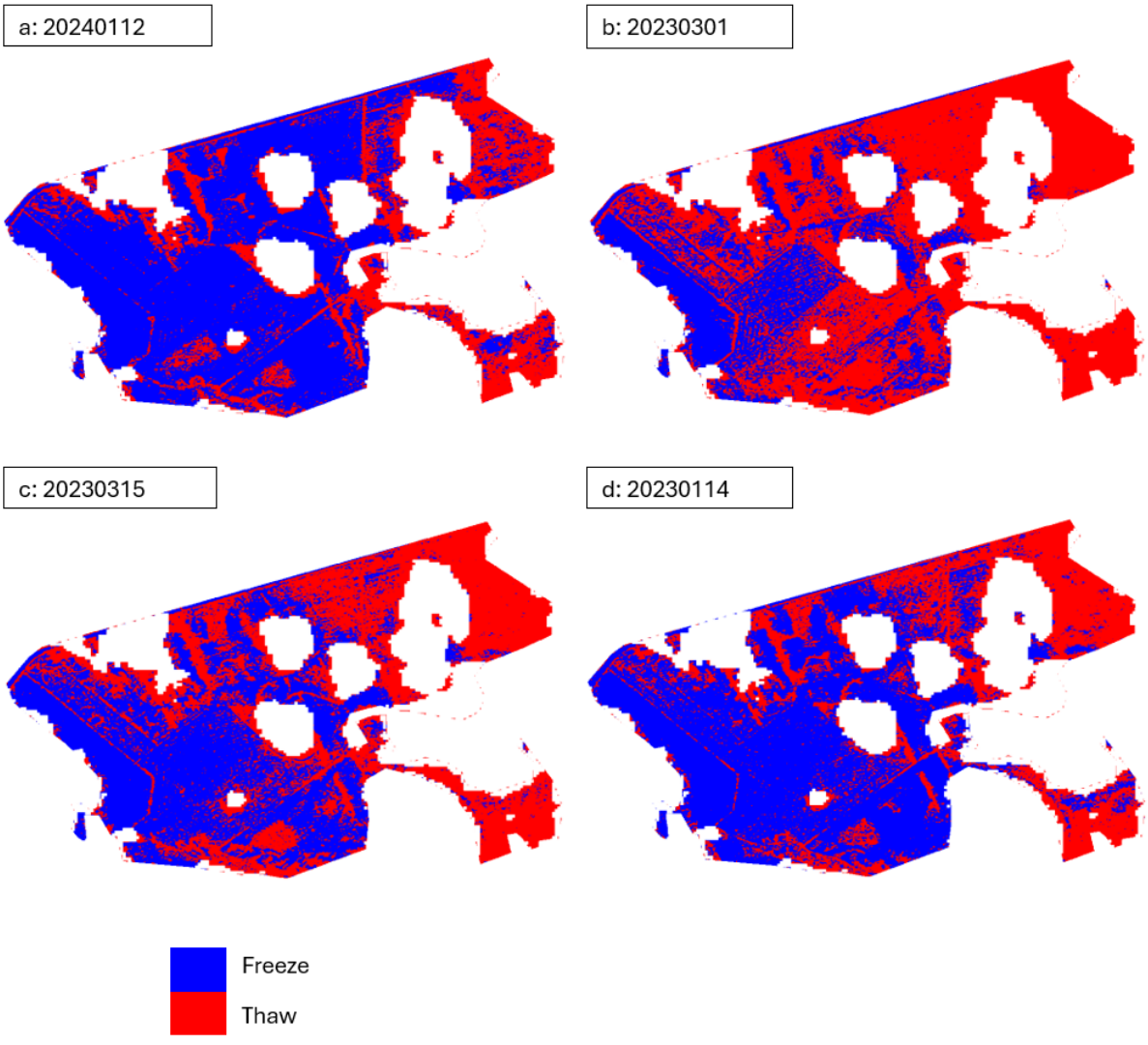

Figure 13. CryoSAR-derived soil F/T maps corresponding to (a) low backscatter response, (b) high backscatter response, (c) low spatial variability, and (d) high spatial variability, based on the dates used for the VV backscatter response.

On March 1st, the soil stations could be considered to be in a thawed state, as indicated by the high VV backscatter response (see Fig. 7), which corresponded well with the soil F/T maps for most of the fields. On 12 January 2024, a very thin snow layer covered the ground, and the lowest backscatter response was observed over the field, supporting the interpretation of a frozen soil state. The soil F/T maps also confirmed the frozen condition on this date.

https://doi.org/10.5194/egusphere-2026-1065
Preprint. Discussion started: 7 April 2026

4 Discussion

4.1 Soil Freeze/Thaw Monitoring using In Situ Observations

The in situ observations captured distinct soil F/T dynamics across the field sites, highlighting the combined influence of temperature, soil moisture, and snowpack. Most stations exhibited consistent frozen conditions from mid-January onward, yet the Winter Rye and Lower sites remained partially thawed for longer periods. This divergence likely reflects differences in vegetation cover and soil texture. The insulating role of snowpack was evident as soil temperatures fluctuated near 0 even when the overlying air was below freezing, delaying the onset of persistent frozen conditions and creating intermittent thaw events later in the season. Soil sensors' records confirm that transitions between frozen and thawed states produce sharp contrasts in dielectric permittivity. The combined temperature–permittivity classification used here reduced misclassification compared to a single-threshold approach, aligning with earlier work showing that dielectric properties provide a more reliable indicator of F/T status than soil temperature alone. Moreover, the thawing event in early January, likely associated with rainfall infiltration and decreased snow cover, agrees with studies linking mid-winter thaws to precipitation.

Data gaps from stations such as East Dry and Upper introduced uncertainty, particularly during periods of frequent F/T cycling. While interpolation using IDW ensured temporal continuity, spatial variability may not have been fully captured. The fixed thresholds applied for classification ($\varepsilon' < 10, T \leq 0$) provide a simplified representation of F/T processes and may not account for intermediate states such as partially frozen soil or snow melt-refreeze events. Additionally, vegetation effects and soil type differences were not explicitly incorporated into the classification framework, despite evidence of their influence on observed site-to-site variability. Despite these limitations, the results have important implications for the validation and calibration of microwave remote sensing observations. The strong dielectric contrasts between frozen and thawed soil highlight the value of in situ dielectric monitoring for supporting L-band SAR applications. The combined threshold approach demonstrated here can reduce false detections in remote sensing products that rely on either temperature or permittivity alone.

Future work should explore adaptive classification schemes that incorporate vegetation and soil type, as well as variable thresholds tuned to local hydrological conditions. Expanding the spatial extent of in situ measurements and coupling them with satellite data (e.g., NISAR) would further improve the robustness of soil F/T monitoring. Incorporating snowpack properties into the classification framework could also enhance interpretation of mid-winter thaw events. Overall, the study demonstrates the necessity of integrating soil permittivity and temperature observations to capture the complexity of F/T processes under variable snow conditions.

4.2 Variability and Magnitude of VV Backscatter

σ^0_{VV} provided clear evidence of soil F/T dynamics throughout the campaign. As expected, VV backscatter was particularly sensitive to changes in soil dielectric properties, showing marked increases during thawing periods and decreases during sustained frozen states. The increasing trends in late January, coincided with rising 2 meter air temperatures and warming of the snowpack layers, confirming the ability of low-frequency L-band VV backscatter to detect soil F/T transitions even under

https://doi.org/10.5194/egusphere-2026-1065
Preprint. Discussion started: 7 April 2026

snow cover. The relatively small magnitude of change at East Dry station compared to Upper and Winter Rye stations suggests localized differences in snow depth, soil type, or microclimatic conditions that buffered the soil from rapid dielectric changes.

These results are consistent with prior studies demonstrating the robustness of VV polarization in detecting soil F/T transitions in seasonally snow-covered environments. Previous work has shown that VV signals penetrate snow more effectively than cross-polarized channels, reducing the confounding influence of vegetation and surface roughness. The observed late-January increases in (σ^0_{VV}) align with the physical expectation of higher dielectric permittivity during thaw, driven by the presence of liquid water in the soil profile. Conversely, the subsequent stabilization or decline in February reflects refreezing and the insulating effect of snow, which dampened further variability in backscatter.

Several considerations must be taken into account when interpreting these backscatter trends. Although vegetation was relatively low and stable during the campaign, even sparse cover may influence scattering mechanisms under certain soil moisture and snow conditions. In addition, while VV is less sensitive to surface roughness than cross-polarized channels, micro-topographic changes and localized compaction under snow cannot be fully excluded as contributors to the observed variability. The spatial differences across stations may also reflect heterogeneity in soil texture, drainage, and snow accumulation patterns, which were not explicitly modeled in this analysis.

These findings confirm the suitability of VV polarization for monitoring soil F/T state in agricultural environments. The ability of VV backscatter to penetrate snow and respond directly to soil dielectric changes provides a valuable basis for calibrating and validating satellite-based L-band SAR observations. Incorporating VV backscatter response with ground-based measurement of soil permittivity and temperature data strengthens the reliability of F/T detection algorithms and reduces false detections caused by vegetation or roughness. Future research should expand on these findings by explicitly quantifying the role of soil type on SAR signal. Continuous multi-year monitoring will also help to capture interannual variability in snow–soil interactions and enhance the robustness of VV-based F/T indicators.

4.3 Changes in Polarimetric Decomposition Parameters

The temporal evolution of surface and volume scattering powers captured by L-band SAR reflects the soil F/T state and associated snow–soil interactions. Surface scattering peaked during periods of consistently frozen soil, such as mid-February, confirming strong backscatter from the frozen ground. In contrast, volume scattering increased during warming periods, particularly in late February and early March, likely driven by snowmelt, melt–refreeze cycles, and ice-layer formation within the snowpack. These trends highlight the sensitivity of volume scattering to liquid water redistribution and structural changes in the snow-soil layer, whereas surface scattering primarily reflects frozen soil conditions or wet snow condition (which was not investigated in this study).

The observed spatial variability of scattering parameters across stations emphasizes the influence of heterogeneous soil type, land cover, and local incidence angles. Despite low vegetation height and winter conditions, elevated volume scattering on certain dates could be related to residual effects of micro-topography and the Freeman–Durden decomposition's tendency to overestimate volume contributions due to depolarization. Comparisons with in situ temperature and permittivity measurements confirm the physical consistency of SAR-derived scattering components with actual soil F/T states, reinforcing the reliability of

https://doi.org/10.5194/egusphere-2026-1065
Preprint. Discussion started: 7 April 2026

model-based polarimetric decomposition for monitoring F/T dynamics. These results suggest that combined analysis of surface and volume scattering can improve detection of F/T transitions under variable snow cover. Surface scattering provides robust indicators of frozen soil, while volume scattering is more responsive to thawing events and snowpack dynamics. Incorporating these insights into operational SAR-based monitoring can improve the interpretation of soil moisture and F/T processes across heterogeneous agricultural landscapes.

4.4 Improved Integral Equation Model

The comparison between CryoSAR observations and I^{2}EM-simulated backscatter indicates that physically-based forward models have limited capability to reproduce soil F/T dynamics when constrained by sparse in situ measurements. Evaluations of I^{2}EM performance at L-band reveal notable discrepancies between modeled and observed backscatter, suggesting that soil F/T analysis relying on this model may be unreliable in the absence of more accurate calibration.

The analysis of L-band airborne SAR data for soil F/T investigation using the I^{2}EM model indicates that fully polarimetric observations are more accurately reproduced in the VV and HV channels, whereas the HH backscatter is substantially underestimated by approximately 9 to 22 dB. Whether this discrepancy arises from intrinsic limitations of the I^{2}EM formulation at L-band HH polarization or from shortcomings in the parameterization of L-band inputs remains open and requires further investigation using additional gravimetric soil measurements, enhanced surface roughness characterization.

These findings confirm that I^{2}EM is unable to reliably capture the dominant changes in winter backscatter in the absence of sufficient gravimetric field data, particularly when backscatter variability is primarily controlled by soil dielectric properties. Discrepancies between predicted and measured values highlight clear limitations of the model. The deviation from the 1:1 line and the elevated RMSE values indicate a pronounced tendency of I^{2}EM to underestimate backscatter, especially in the HH channel. Comparable biases have been reported in previous IEM-based studies, where depolarization effects associated with surface roughness and vegetation were not fully represented.

The observed backscatter errors were primarily associated with surface roughness, a key factor governing electromagnetic scattering at the soil surface, as well as with the parameterization of the Dobson (1985) dielectric mixing model using a single gravimetric soil measurement. Uncertainties related to surface roughness, including measurement errors, spatial heterogeneity, and reliance on single-time observations, together with one-time gravimetric soil sampling prior to the snow-on period, have been identified as major contributors to the model's inability to reproduce backscatter measurements from airborne sensor. Furthermore, the use of a single UAV-based roughness measurement, although operationally practical, may have introduced additional uncertainty by failing to capture temporal variability across the study site. Future improvements should prioritize enhanced model parameterization through more intensive ground-based observations and the integration of dynamic roughness measurements to better represent complex scattering processes.

4.5 CryoSAR-derived Freeze/Thaw Maps

Figure 13 presents examples of the retrieved F/T soil states derived from CryoSAR airborne measurements at a spatial resolution of 1×1 m, during the transition from frozen to thawed conditions. Figure 13-a shows a predominantly frozen state of the

https://doi.org/10.5194/egusphere-2026-1065
Preprint. Discussion started: 7 April 2026

soil, while Fig. 13-b shows a mostly thawed state. Fig. 13-c and Fig. 13-d illustrate areas with low and high spatial variability across the study region, respectively.

On the western side of the field, the algorithm classified most areas as frozen, which is consistent with field conditions, as the stations were located in open fields with little to no vegetation cover, enabling rapid soil freezing. Although tree biomass was not expected to contribute substantially to backscatter sensitivity of L-band SAR, the central part of the field exhibited some influence from trees and branches. Because tree biomass freezes less than soil, the algorithm classified these areas as thawed.

5 Conclusions

There is limited understanding of how lower-frequency backscatter and polarimetric parameters, such as L-band SAR, respond to soil F/T transitions under snow-covered conditions, particularly when validated against comprehensive ground-based soil and weather measurements. To address this gap, this study analyzed a season-long time series of airborne L-band SAR observations over a well-instrumented study area. Unlike previous work that relied mainly on coarser-resolution C-band SAR data, this research focuses on high-resolution ($1 \times 1\,\mathrm{m}$) L-band imagery, providing an opportunity to assess whether lower-frequency SAR at fine spatial scales can effectively capture F/T transitions. By linking soil temperature and moisture dynamics to VV backscatter and polarimetric decomposition results, we isolated the contributions of surface and volume scattering under frozen and thawed conditions. Finally, the I^2EM forward model was employed to retrieve soil state and map its spatial distribution, demonstrating a physically based approach for L-band F/T monitoring.

Airborne L-band SAR data from the 2023 and 2024 winter seasons were used to examine soil F/T conditions. Due to warmer-than-average temperatures and significantly reduced snowfall, only two datasets were acquired for the winter 2023–2024 period, which experienced milder conditions than a typical Ontario winter. Despite this, time-series analysis of in situ soil station and nearby weather station data confirmed that both the backscatter response and the Freeman–Durden-derived surface and volume scattering components captured seasonal changes in soil state. The results showed a general decrease in backscatter as temperatures dropped below freezing, consistent with in situ observations. Volume scattering dominated during thaw periods, while frozen soil conditions were characterized by increased surface scattering.

These findings highlight opportunities for further investigation into the use of polarimetric decomposition and physically based models such as I^2EM for soil F/T detection. In particular, incorporating temporally resolved surface roughness and gravimetric soil measurements may improve model parameterization and enhance the accuracy of simulated backscatter. Additionally, detailed characterization of vegetation type, height, and snow-covered canopy conditions could help explain variations in decomposition response. Finally, future research should explore how melt–refreeze cycles and evolving snowpack conditions influence both backscatter behavior and decomposition dynamics. This study was conducted in winter, when vegetation cover was minimal. Under conditions with denser vegetation, mapping frozen areas would likely be more challenging, particularly when temperatures hover just below $0\,^{\circ}\mathrm{C}$, as the contrast in backscatter between frozen and unfrozen surfaces tends to decrease.

https://doi.org/10.5194/egusphere-2026-1065
Preprint. Discussion started: 7 April 2026

Appendix A

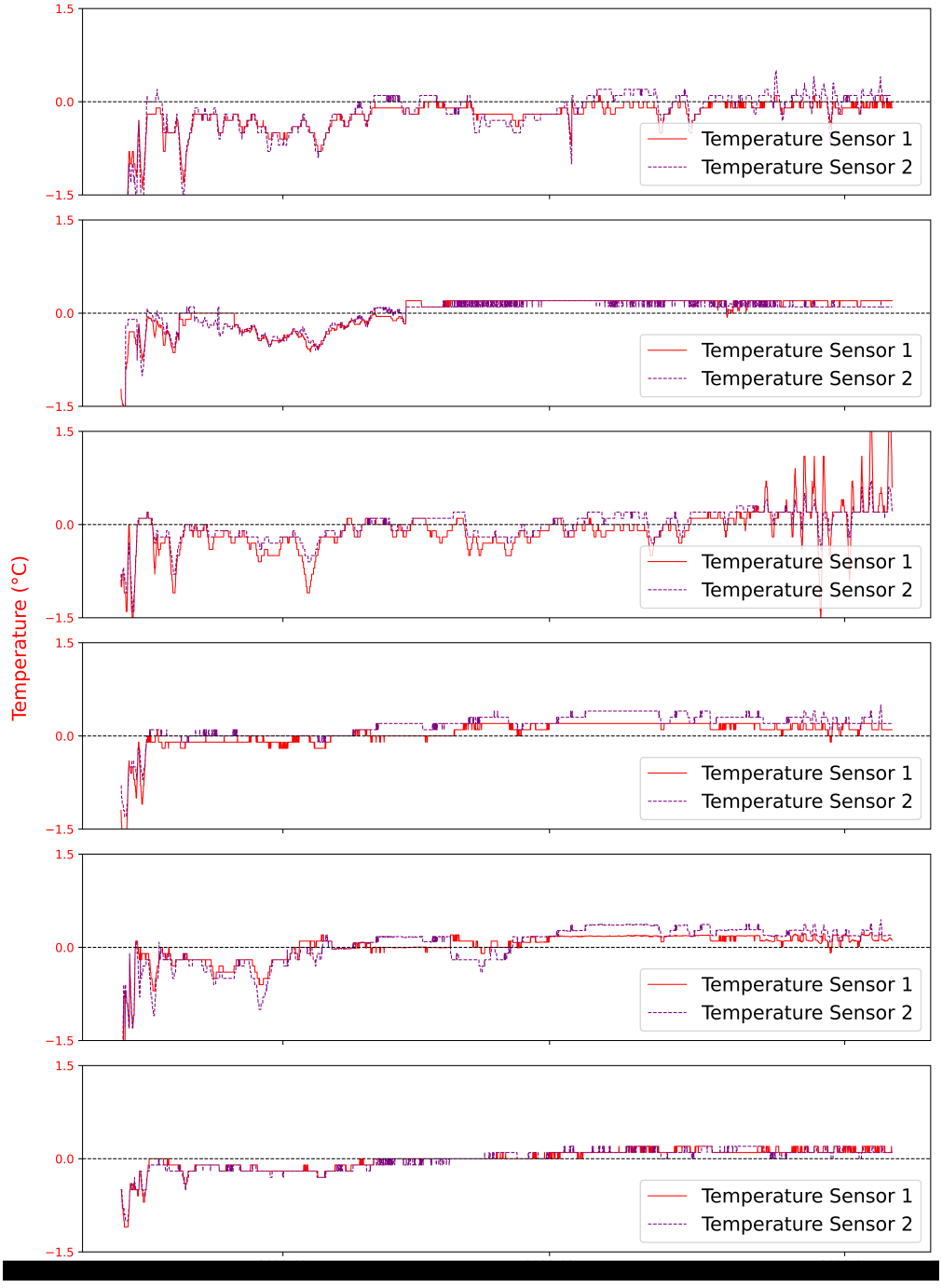

Figure A1. Time-series of soil temperatures

https://doi.org/10.5194/egusphere-2026-1065
Preprint. Discussion started: 7 April 2026

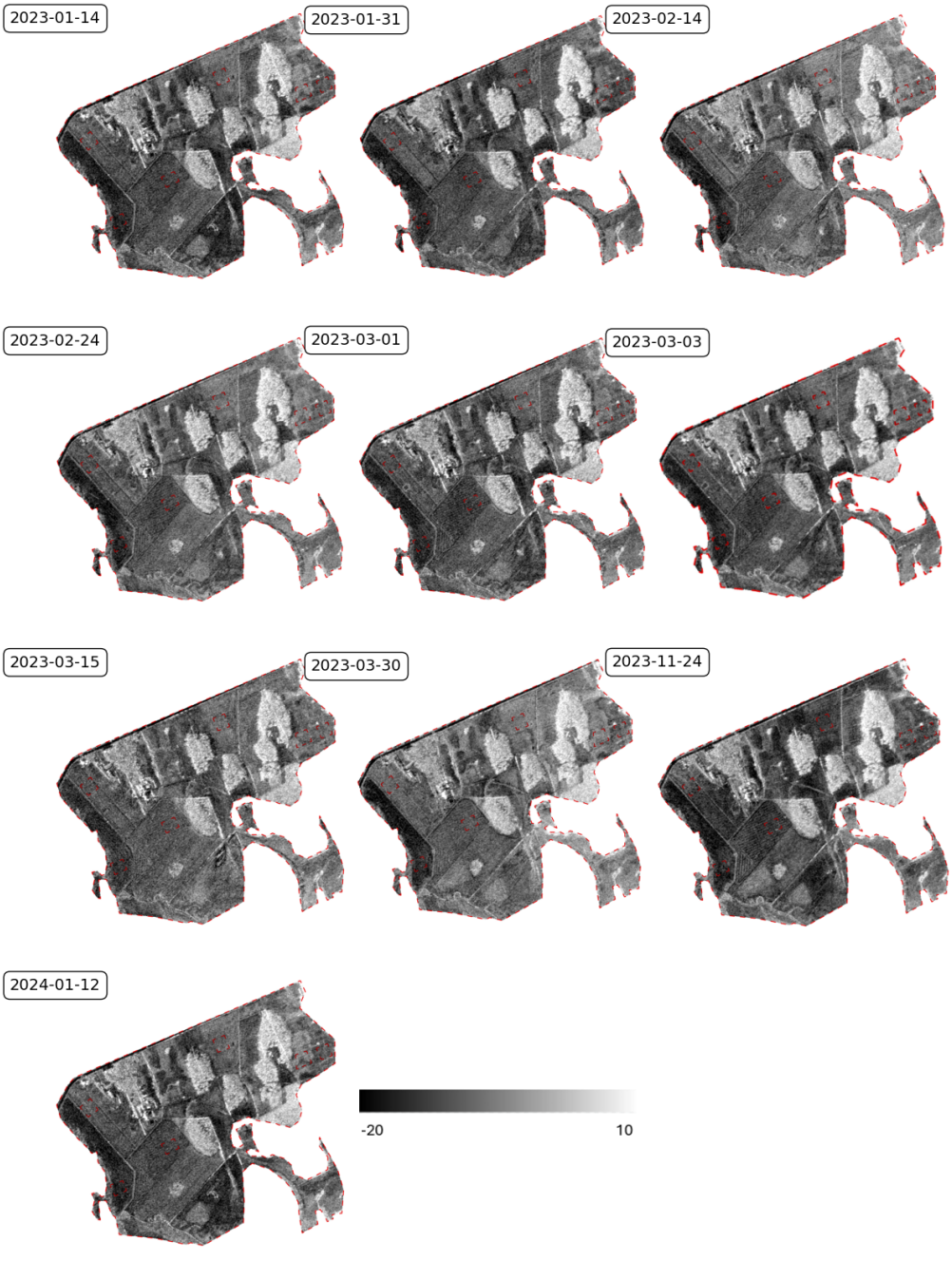

Figure A2. Temporal variability of co-polarization VV backscatter observed throughout the CryoSAR field campaign. The plot illustrates changes in VV polarization over the study site, highlighting spatial and temporal fluctuations during the measurement period.

https://doi.org/10.5194/egusphere-2026-1065
Preprint. Discussion started: 7 April 2026

Acknowledgements. The authors would like to thank the field participants, Arvids Silis, Mike Davey (Environment and Climate Change Canada), Jeffrey Welch, and Lina Zschenderlein (University of Waterloo), for their valuable assistance in data collection. The authors also acknowledge gratefully Markus Wand for providing access to the Wand Family Farm and supporting the field experiments.

Author contributions. Zeinab Akhavan: Conceptualization, Data curation, Formal analysis, Investigation, Methodology, Software, Validation, Visualization, Writing – original draft, Writing – review editing. Richard Kelly: Conceptualization, Funding acquisition, Methodology, Project administration, Supervision, Writing – review editing. Peter Toose: Data curation, Writing – review editing. Aaron Thompson: Writing – review editing. Wei Wang: Data curation. Benoit Montpetit: Writing – review editing. Alex Gélinas: Data curation, Writing – review editing. Alexandre Roy: Writing – review editing.

Code and data availability. The data supporting the findings of this study and codes used for data processing and analysis are not publicly available at this time but are available from the corresponding author upon request.

Competing interests. The authors declare that they have no competing interests.

https://doi.org/10.5194/egusphere-2026-1065
Preprint. Discussion started: 7 April 2026

References

Akhavan, Z., Hasanlou, M., Hosseini, M., and McNairn, H.: Decomposition-based soil moisture estimation using UAVSAR fully polarimetric images, Agronomy, 11, 145, https://doi.org/https://doi.org/10.3390/agronomy11010145, 2021.

Baghdadi, N., Saba, E., Aubert, M., Zribi, M., and Baup, F.: Evaluation of radar backscattering models IEM, Oh, and Dubois for SAR data in X-band over bare soils, IEEE Geoscience and Remote Sensing Letters, 8, 1160–1164, https://doi.org/https://doi.org/10.1109/LGRS.2011.2158982, 2011.

Bahrami, H., Homayouni, S., McNairn, H., Hosseini, M., and Mahdianpari, M.: Regional crop characterization using multi-temporal optical and synthetic aperture radar earth observations data, Canadian Journal of Remote Sensing, 48, 258–277, https://doi.org/https://doi.org/10.1080/07038992.2021.2011180, 2022.

Bateni, S. M., Margulis, S. A., Podest, E., and McDonald, K. C.: Characterizing snowpack and the freeze–thaw state of underlying soil via assimilation of multifrequency passive/active microwave data: A case study (NASA CLPX 2003), IEEE Transactions on Geoscience and Remote Sensing, 53, 173–189, https://doi.org/https://doi.org/10.1109/TGRS.2014.2320264, 2015.

Cohen, J., Rautiainen, K., Lemmetyinen, J., Smolander, T., Vehviläinen, J., and Pulliainen, J.: Sentinel-1 based soil freeze/thaw estimation in boreal forest environments, Remote Sensing of Environment, 254, 112 267, https://doi.org/https://doi.org/10.1016/j.rse.2020.112267, 2021.

Crevier, C., Langlois, A., Derksen, C., and Roy, A.: A mutlisensor C-band synthetic aperture radar (SAR) approach to retrieve freeze/thaw cycles: A case study for a low Arctic environment, EGUsphere, 2025, 1–26, https://doi.org/https://doi.org/10.5194/egusphere-2024-3580, 2025.

Dagurov, P., Chimitdorzhiev, T., Dmitriev, A., and Dobrynin, S.: Estimation of snow water equivalent from L-band radar interferometry: simulation and experiment, International Journal of Remote Sensing, 41, 9328–9359, https://doi.org/https://doi.org/10.1080/01431161.2020.1798551, 2020.

De Macedo, K. A., Masalias, G., Coccia, A., and Meta, A.: Recent LC-and X-band MetaSensing airborne SAR campaigns for emerging applications, in: 2020 17th European Radar Conference (EuRAD), pp. 190–193, IEEE, https://doi.org/https://doi.org/10.1109/EuRAD48048.2021.00056, 2021.

Deeb, E. J., Forster, R. R., and Kane, D. L.: Monitoring snowpack evolution using interferometric synthetic aperture radar on the North Slope of Alaska, USA, International journal of remote sensing, 32, 3985–4003, https://doi.org/https://doi.org/10.1080/01431161003801351, 2011.

Derksen, C., Xu, X., Dunbar, R. S., Colliander, A., Kim, Y., Kimball, J. S., Black, T. A., Euskirchen, E., Langlois, A., Loranty, M. M., et al.: Retrieving landscape freeze/thaw state from Soil Moisture Active Passive (SMAP) radar and radiometer measurements, Remote Sensing of Environment, 194, 48–62, https://doi.org/https://doi.org/10.1016/j.rse.2017.03.007, 2017.

Dobson, M. C., Ulaby, F. T., Hallikainen, M. T., and El-Rayes, M. A.: Microwave dielectric behavior of wet soil-Part II: Dielectric mixing models, IEEE Transactions on geoscience and remote sensing, pp. 35–46, https://doi.org/https://doi.org/10.1109/TGRS.1985.289498, 2007.

Du, J., Shi, J., and Rott, H.: Comparison between a multi-scattering and multi-layer snow scattering model and its parameterized snow backscattering model, Remote Sensing of Environment, 114, 1089–1098, https://doi.org/https://doi.org/10.1016/j.rse.2009.12.020, 2010.

Dubois, P. C., Van Zyl, J., and Engman, T.: Measuring soil moisture with imaging radars, IEEE transactions on geoscience and remote sensing, 33, 915–926, https://doi.org/https://doi.org/10.1109/TGRS.1995.477194, 1995.

https://doi.org/10.5194/egusphere-2026-1065
Preprint. Discussion started: 7 April 2026

Environment and Climate Change Canada: Climate Normals for Powassan, https://climate.weather.gc.ca/climate_normals/results_1981_2010_e.html?searchType=stnName&txtStationName=powassan, 1981–2010 Climate Normals, 2024.

Freeman, A. and Durden, S. L.: A three-component scattering model for polarimetric SAR data, IEEE transactions on geoscience and remote sensing, 36, 963–973, https://doi.org/https://doi.org/10.1109/36.673687, 2002.

Fung, A. K., Li, Z., and Chen, K.-S.: Backscattering from a randomly rough dielectric surface, IEEE Transactions on Geoscience and remote sensing, 30, 356–369, https://doi.org/https://doi.org/10.1109/36.134085, 1992.

Fung, A. K., Liu, W., Chen, K., and Tsay, M.: An improved IEM model for bistatic scattering from rough surfaces, Journal of Electromagnetic Waves and Applications, 16, 689–702, https://doi.org/https://doi.org/10.1163/156939302X01119, 2002.

Hajnsek, I. and Desnos, Y.-L.: Polarimetric synthetic aperture radar: principles and application, vol. 25, Springer Nature, https://doi.org/https://doi.org/10.1007/978-3-030-56504-6, 2021.

Hänsch, R., Jagdhuber, T., and Fersch, B.: Soil-permittivity estimation under grassland using machine-learning and polarimetric decomposition techniques, IEEE Transactions on Geoscience and Remote Sensing, 59, 2877–2887, https://doi.org/https://doi.org/10.1109/TGRS.2020.3010104, 2020.

Holah, N., Baghdadi, N., Zribi, M., Bruand, A., and King, C.: Potential of ASAR/ENVISAT for the characterization of soil surface parameters over bare agricultural fields, Remote sensing of environment, 96, 78–86, https://doi.org/https://doi.org/10.1016/j.rse.2005.01.008, 2005.

Inoubli, R., Constantino-Recillas, D. E., Monsiváis-Huertero, A., Farah, L. B., and Farah, I. R.: Assessment of Surface Scattering Models within the Water Cloud Model Towards Soil Moisture Retrievals using Sentinel-1 and Sentinel-2 Images, IEEE Journal of Selected Topics in Applied Earth Observations and Remote Sensing, https://doi.org/https://doi.org/10.1109/JSTARS.2024.3462591, 2024.

Jagdhuber, T., Stockamp, J., Hajnsek, I., and Ludwig, R.: Identification of soil freezing and thawing states using SAR polarimetry at C-band, Remote Sensing, 6, 2008–2023, https://doi.org/https://doi.org/10.3390/rs6032008, 2014.

Karam, M. A., Fung, A. K., Lang, R. H., and Chauhan, N. S.: A microwave scattering model for layered vegetation, Universities Space Research Association, Goddard Visiting Scientist Program for the Space and Earth Sciences Directorate, 1992.

Kelly, R., Thompson, A., Wang, W., Akhavan, Z., Welch, J., Toose, P., Derksen, C., Montpetit, B., and Meta, A.: The Airborne Cryospheric SAR System (CryoSAR): Characterizing Cold Season Hydrology Using Ku and L-Band Polarimetric SAR Observations, in: IGARSS 2024-2024 IEEE International Geoscience and Remote Sensing Symposium, pp. 6559–6561, IEEE, https://doi.org/https://doi.org/10.1109/IGARSS53475.2024.10642350, 2024.

Kim, Y., Kimball, J. S., Glassy, J., and Du, J.: An extended global Earth system data record on daily landscape freeze–thaw status determined from satellite passive microwave remote sensing, Earth System Science Data, 9, 133–147, https://doi.org/https://doi.org/10.5194/essd-9-133-2017, 2017.

Lee, J.-S. and Pottier, E.: Polarimetric radar imaging: from basics to applications, CRC press, https://doi.org/https://doi.org/10.1201/9781420054989, 2017.

Lievens, H., Brangers, I., Marshall, H.-P., Jonas, T., Olefs, M., and De Lannoy, G.: Sentinel-1 snow depth retrieval at sub-kilometer resolution over the European Alps, The Cryosphere, 16, 159–177, https://doi.org/https://doi.org/10.5194/tc-16-159-2022, 2022.

Long, D. and Ulaby, F.: Microwave radar and radiometric remote sensing, Artech, 2015.

Marshall, H.-P., Deeb, E., Forster, R., Vuyovich, C., Elder, K., Hiemstra, C., and Lund, J.: L-band InSAR depth retrieval during the NASA SnowEx 2020 campaign: Grand mesa, Colorado, pp. 625–627, https://doi.org/https://doi.org/10.1109/IGARSS47720.2021.9553852, 2021.

Mätzler, C.: Applications of the interaction of microwaves with the natural snow cover, Remote sensing reviews, 2, 259–387, 1987.

https://doi.org/10.5194/egusphere-2026-1065
Preprint. Discussion started: 7 April 2026

Mavrovic, A., Roy, A., Royer, A., Filali, B., Boone, F., Pappas, C., and Sonnentag, O.: Dielectric characterization of vegetation at L band using an open-ended coaxial probe. Geoscientific Instrumentation Methods and Data Systems 7: 195–208, https://doi.org/https://doi.org/10.5194/gi-7-195-2018, 2018.

Mavrovic, A., Sonnentag, O., Lemmetyinen, J., Voigt, C., Rutter, N., Mann, P., Sylvain, J.-D., and Roy, A.: Environmental controls of winter soil carbon dioxide fluxes in boreal and tundra environments, Biogeosciences, 20, 5087–5108, https://doi.org/https://doi.org/10.5194/bg-20-5087-2023, 2023.

Mavrovic, A., Sonnentag, O., Lemmetyinen, J., Voigt, C., Aurela, M., and Roy, A.: Winter methane fluxes over boreal and Arctic environments, Authorea Preprints, https://doi.org/https://doi.org/10.22541/essoar.170542245.58670859/v1, 2024.

Moreira, A., Prats-Iraola, P., Younis, M., Krieger, G., Hajnsek, I., and Papathanassiou, K. P.: A tutorial on synthetic aperture radar, IEEE Geoscience and remote sensing magazine, 1, 6–43, https://doi.org/https://doi.org/10.1109/MGRS.2013.2248301, 2013.

Oh, Y., Sarabandi, K., and Ulaby, F. T.: An empirical model and an inversion technique for radar scattering from bare soil surfaces, IEEE transactions on Geoscience and Remote Sensing, 30, 370–381, https://doi.org/https://doi.org/10.1109/36.134086, 2002.

Palomaki, R. T. and Sproles, E. A.: Assessment of L-band InSAR snow estimation techniques over a shallow, heterogeneous prairie snowpack, Remote Sensing of Environment, 296, 113 744, https://doi.org/https://doi.org/10.1016/j.rse.2023.113744, 2023.

Panciera, R., Tanase, M. A., Lowell, K., and Walker, J. P.: Evaluation of IEM, Dubois, and Oh radar backscatter models using airborne L-band SAR, IEEE Transactions on Geoscience and Remote Sensing, 52, 4966–4979, https://doi.org/https://doi.org/10.1109/TGRS.2013.2286203, 2013.

Park, S.-E.: Variations of microwave scattering properties by seasonal freeze/thaw transition in the permafrost active layer observed by ALOS PALSAR polarimetric data, Remote Sensing, 7, 17 135–17 148, https://doi.org/https://doi.org/10.3390/rs71215874, 2015.

Prince, M., Roy, A., Royer, A., and Langlois, A.: Timing and spatial variability of fall soil freezing in boreal forest and its effect on SMAP L-band radiometer measurements, Remote Sensing of Environment, 231, 111 230, https://doi.org/https://doi.org/10.1016/j.rse.2019.111230, 2019.

Rowlandson, T. L., Berg, A. A., Roy, A., Kim, E., Lara, R. P., Powers, J., Lewis, K., Houser, P., McDonald, K., Toose, P., et al.: Capturing agricultural soil freeze/thaw state through remote sensing and ground observations: A soil freeze/thaw validation campaign, Remote sensing of environment, 211, 59–70, https://doi.org/https://doi.org/10.1016/j.rse.2018.04.003, 2018.

Shi, J., Xiong, C., and Jiang, L.: Review of snow water equivalent microwave remote sensing, Science China Earth Sciences, 59, 731–745, https://doi.org/https://doi.org/10.1007/s11430-015-5225-0, 2016.

Singh, S. K., Prasad, R., Srivastava, P. K., Yadav, S. A., Yadav, V. P., and Sharma, J.: Incorporation of first-order backscattered power in Water Cloud Model for improving the Leaf Area Index and Soil Moisture retrieval using dual-polarized Sentinel-1 SAR data, Remote Sensing of Environment, 296, 113 756, https://doi.org/https://doi.org/10.1016/j.rse.2023.113756, 2023.

Tao, L., Li, J., Chen, X., Cai, Q., and Zhang, Y.: An effective model to retrieve soil moisture from L-and C-band SAR data, Journal of the Indian Society of Remote Sensing, 45, 621–629, https://doi.org/https://doi.org/10.1007/s12524-016-0626-x, 2017.

Thompson, A. and Kelly, R.: Considerations for Ku-Band Radar Retrieval of Snow Water Equivalent at Mid-Latitude Ontario Agricultural Sites, Canadian Journal of Remote Sensing, 47, 119–142, https://doi.org/https://doi.org/10.1080/07038992.2021.1898938, 2021.

Tsang, L., Durand, M., Derksen, C., Barros, A. P., Kang, D.-H., Lievens, H., Marshall, H.-P., Zhu, J., Johnson, J., King, J., et al.: Global monitoring of snow water equivalent using high frequency radar remote sensing, The Cryosphere Discussions, 2021, 1–57, https://doi.org/https://doi.org/10.5194/tc-16-3531-2022, 2021.

https://doi.org/10.5194/egusphere-2026-1065
Preprint. Discussion started: 7 April 2026

Turkar, V. and Rao, Y.: Applying coherent and incoherent target decomposition techniques to polarimetric SAR data, in: Proceedings on the IJCA International Conference on Technology Systems and Management, pp. 23–29, 2011.

Wang, H., Magagi, R., and Goita, K.: Comparison of different polarimetric decompositions for soil moisture retrieval over vegetation covered agricultural area, Remote Sensing of Environment, 199, 120–136, https://doi.org/https://doi.org/10.1016/j.rse.2017.07.008, 2017.

Zeng, J. and Chen, K.-S.: Theoretical study of global sensitivity analysis of L-band radar bistatic scattering for soil moisture retrieval, IEEE Geoscience and Remote Sensing Letters, 15, 1710–1714, https://doi.org/https://doi.org/10.1109/LGRS.2018.2858269.

Zhang, X., Chen, B., Zhao, H., Li, T., and Chen, Q.: Physical-based soil moisture retrieval method over bare agricultural areas by means of multi-sensor SAR data, International Journal of Remote Sensing, 39, 3870–3890, https://doi.org/https://doi.org/10.1080/01431161.2018.1452072, 2018.

Zhou, X., Zhang, Z., Shen, Q., Chen, Q., and Liu, X.: Identifying soil freeze/thaw states using scattering and coherence time series of high-resolution C-band synthetic aperture radar in the Qinghai-Tibet Plateau, IEEE Journal of Selected Topics in Applied Earth Observations and Remote Sensing, 15, 519–532, https://doi.org/10.1109/JSTARS.2021.3137187, 2021.

Zribi, M., Chahbi, A., Shabou, M., Lili-Chabaane, Z., Duchemin, B., Baghdadi, N., Amri, R., and Chehbouni, A.: Soil surface moisture estimation over a semi-arid region using ENVISAT ASAR radar data for soil evaporation evaluation, Hydrology and Earth System Sciences, 15, 345–358, https://doi.org/https://doi.org/10.5194/hess-15-345-2011, 2011.